Structural And Dielectric Study Of SiO_2 Coated $ZnFe_2O_4$ Nanoparticles

SUPERIOR UNIVERSITY

Thesis Submitted to

The Superior University Lahore

In Partial Fulfilment of the

Requirement for the Degree of

Master of Philosophy in Chemistry

By

MUQADDAS WASEEM

Roll No. MSCHE-S22-002

Session: 2022-2024

Faculty of Sciences

Author's Declaration

I hereby state that my M.Phil. Thesis titled **"Structural and dielectric study of SiO_2 coated $ZnFe_2O_4$ nanoparticles"** is my work and has not been submitted previously by me for taking any degree from this University,

The Superior University, Lahore,

or anywhere else in the country/world.

At any time if my statement is found to be incorrect even after my graduation, the university has the right to withdraw my M.Phil. degree.

Student Name: Muqaddas Waseem

Date: _____

Plagiarism Undertaking

I solemnly declare that the research work presented in the thesis titled **"Structural and dielectric study of SiO_2 coated $ZnFe_2O_4$ nanoparticles"** is solely my research work with no significant contribution from any other person.

Small contribution/help wherever taken has been duly acknowledged and that complete thesis has been written by me.

I understand the zero-tolerance policy of the HEC and University,

The Superior University, Lahore,

Towards plagiarism. Therefore, I as the author of the above-titled thesis declare that no portion of my thesis has been plagiarized and any material used as a reference is properly referred/cited. I undertake that if I am found guilty of any formal plagiarism in the above-titled thesis, even after awarding of an M.Phil. degree, the University reserves the right to withdraw/revoke my M.S degree and that HEC and the University have the right to publish my name on the HEC/University website on which names of students are placed who submitted a plagiarized thesis.

Student/Author Signature: _____

Name: Muqaddas Waseem

Research Completion Certificate

This is to certify that the thesis entitled **"Structural and dielectric study of SiO_2 coated $ZnFe_2O_4$ nanoparticles"** submitted by **"Muqaddas Waseem''** has been accepted towards the partial fulfillment of the requirement for M.Phil. "**Chemistry**". The quality of the work contained in this thesis is adequate for the award of a degree.

Name of Supervisor: Dr. Fiza Naseem

Designation: Assistant Professor

Signature: _____

CERTIFICATE OF APPROVAL

This is to certify that the research work presented in this thesis, titled "**In-House Method Validation of the Herbicide Cyhalofop-Buutyl by HPLC and its In-Vivo Toxicological Investigations**" was conducted by "**Komal Zehra**" under the supervision of "**Mr**. **Haroon Riaz**". No part of this thesis has been submitted anywhere else for any other degree. This thesis is submitted to the Faculty of Sciences, The Superior University, Lahore in partial fulfillment of the requirements for the degree of Master of Philosophy in the field of "**Chemistry**" in the Faculty of Sciences at The Superior University, Lahore.

Student: Komal Zehra: Signature: _____

Examination Committee:

Session Chair: Dr. M. Mudassir Iqbal Signature: _____

a) External Examiner: Dr. Dure Najaf Iqbal Signature: _____

Associate Professor

Department of Chemistry

University of Lahore

b) Internal Examiner: Dr. Fizza Naseem Signature: _____

c) Supervisor: Mr. Haroon Riaz Signature: _____

c) Co-Supervisor: Mr. Irfan Naseer Signature: _____

d) HOD: Prof. Dr. Uqba Mehmood Signature: _____

e) Dean: Prof. Dr. Mohammad Naveed Babur Signature: _____

f) Controller Examination: Dr. Muhammad Haris Signature: _____

_____

Dedication

This thesis is wholeheartedly dedicated to my beloved parents and my respected teacher, who have been our source of inspiration and gave strength when he thought giving up, who continually provide their moral, spiritual, emotional, and financial support.

And lastly, we dedicated this thesis to the Almighty God, thank you for the guidance, strength, power of mind, protection and skills and for giving us a healthy life. All of these we offer to you.

Acknowledgments

First, I own my deepest gratitude to **Allah Almighty** for all of his countless blessings. I offer my humblest word of thanks to HIS most noble messenger **Hazrat Muhammad (P.B.U.H)**, who is forever, a torch of guidance and knowledge for all humanity. By virtue of his blessing today I can carry out our research work and present it.

Secondly, I would like to thank my respected teacher and supervisor, **Dr. Fizza Naseem,** Department of Chemistry, The superior university, Lahore, whose worthy guidance and professional attitude is appreciable in completing this dissertation. I am also thankful to Head of Department **Dr**. **Uqba Mehmood** and program **Leader Dr. Mudassir Iqbal** for providing facilities to carry out this research work.

I thankfully acknowledge the support and inspiration that I received from my co-supervisor especially **Dr. Muhammad Mubashir and Dr. Liaqat Ali**, **Sir Nazaqat Ali**. It was impossible to complete this hard task of my life. Without his guidance it was not possible for me to complete my MS. Almighty **Allah** blessed them in every part of life

I shall also pay attribute to Hazrat Sian Muhammad Yousaf and Noor Muhammad and Muhammad Ashraf for their prayers, their carrying encouragement and their guidance and enlightens for me. I am deeply grateful to my beloved father Muhammad waseem and loving Mother Zahida Waseem, and loving sisters Dr. Wahdat Waseem, Dr. Saira Waseem, Rabia Waseem and all cousins for their encouragement, support and confidence on me, for their support appreciation, encouragement and keen interest in my academic achievement It was impossible to complete this work without their efforts.

TABLE OF CONTENTS

LIST OF TABLES

Description **Page**

LIST OF FIGURES

Description **Page**

ABSTRACT

Using the sol gel process, Zinc ferrite nanoparticles embedded in a SiO_2 matrix (y = 0, 5, 10, 15, and 20 wt. % of total nitrates) were synthesized. Energy dispersive X- ray spectroscopy (EDX), scanning electron microscopy (SEM), X-ray diffraction (XRD), and LCR meters have all been used to investigate the impact of the SiO_2 matrix on the structural and dielectric properties of zinc ferrite nanoparticles. X-ray diffraction technique (XRD) was used to analyze the single-phase cubic Structure, the purity of phase, and the crystalline size of material. The scanning electron microscopy (SEM) technique was used to investigate the morphology of nanoparticles, that had of spherical, rod and as well as irregular shape due to agglomeration and segregation of these nanoparticles. The EDX spectrum used to indicate the presence of Zn, Fe, O, C, and Si in the examined sample. Using LCR meter, dielectric properties were investigated in the frequency range of 100 Hz to 10 MHz. The value of dielectric constants and loss tangent gradually found to decrease with increase in frequency and eventually became constant at higher frequencies. Conductivity, on the other hand, exhibits the reverse pattern and was more valuable at higher frequencies. The Maxwell-Wagner model and Koop's theory had been used to explain dielectric properties. Hence the structural and dielectric properties of zinc ferrite nanoparticles are significantly influenced by the quantity of SiO_2.

CHAPTER 1

INTRODUCTION

1.1 Nanoscience

Nanoscience concerns the analyzing of procedure and composition of material and molecules at atomic level. The prospect of substances at nanoscales are changed to a large extent of material.

1.1.1 Nanotechnology

Nanotechnology is defined as technology that distributes the particle range between the ranges of 1 to 100 nm. Nanotechnology contains scheming, description, construction by specifying its design of substance and gadget and order by managing the configuration and dimension of material [1].

1.1.2 History

The Greek term for dwarf is nano. Richard Feynman introduced the concepts of nanoscience and nanotechnology for the first time in 1959 [2]. Tokyo University's Norio Taniguchi introduced the term "nanotechnology" in 1983. The dimensions, forms, and characteristics of bulk and nanomaterials differ.

1.1.3 Introduction To Nanotechnology

Nanoscales are one billionth (10^{-9}) of a meter. Nanomaterials have excessive area to volume ratio which assemble components well known at nanoscales. In this case, single atoms in the circumstance of metal are not conducting, however large metallic substances have contemplating nature. Materials get extra remarkable when the dimension of substance become less to nano meter spectrum. Components have extremely favorable characteristics in the instance of one, two-, and three-dimension substances along with nano meter (nm) categories. Therefore, the prospect of these components isn’t the same in the sense of large components [3]. As the dimension of substance declines to shorter than in 50 nm ratio of surface area to volume gets larger. Magnetic reminiscence of nano substance revolves around its size [4]. If the constitution and construction of material and devices can be managed at nanometer scale, then we get substance with new objectives thus enhancing the production of materials.

Figure 1.1 Shows (a) SEM image of zero-dimension (b) 1-dimensional SEM image nanoparticles (c) 2-dimensional nanoparticles shown in an SEM image.

zero-dimensional material [5]	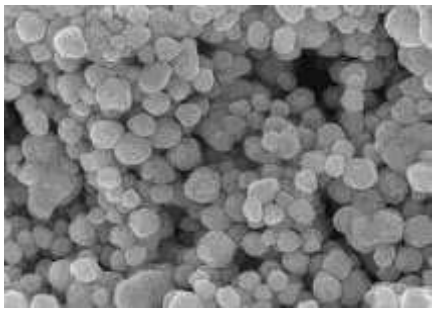 (a)
1-dimensional material [6]	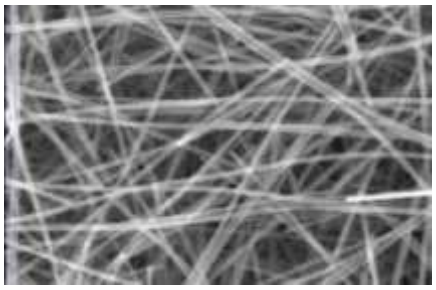 (b)
2-dimensional material [7]	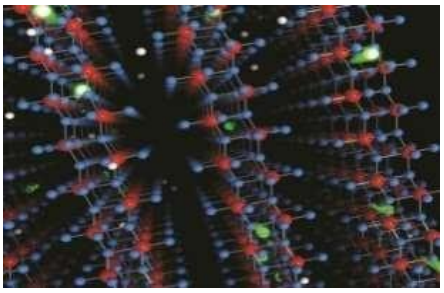 (c)

Figure 1.1: (a) Zero dimensional [5], (b) 1-dimensional [6], (c) 2-dimensional [7] materials.

Materials with nanostructure have been avid attentiveness for scientists due to their tremendous performance in region of industry, biomedical and electrical equipment application. Polycrystalline with extent of nanometer range (1-100 nm) are termed as nanocrystals which boosted their distinct prospects such as ductility, solidity, sharpness, electronic and voltaic properties [8]. Nano crystals are a combination of

atoms among crystalline matter called clusters on a scale of 10-15 nm. All branches of research, including physics, chemistry, medicine, and engineering, have collaborated on projects related to nanotechnology**.** Because of its wide range of applications in electronics, energy, storage devices, environments, optics, nanocoating's, comforts, electrochemistry, quells, magnetism, nanomedicine, biosensors, nanotubes, aerospace, nano catalyst, high energy batteries, and Nano fillers, scientists become concerned when they come into contact with nanomaterials or nanostructure.

1.1.4 Nanoparticles

Nanoparticles are defined as particles with a radius between 1-100 nm. Nanoparticles can take the form of colloids, clusters, or nanocrystals. Super anticipating characteristics set nanoparticles apart from most particles. At nanoscales the area diminishes particles and its features like electrical, mechanical, optical, and various properties change theatrically.

At nanoscales magnetic qualities of nanoparticles are diverged than huge material. The ferromagnetism of nanoparticles changes to superparamagnetic when their particle number falls below 100 nm. This is because the increased surface to volume ratio increases the surface efficiency of the nanoparticles. In advancement of nanotechnology all areas of science have uniform contribution

1.2 Magnetism And Its Concepts

Force of repulsion or attraction of magnetic substance by ranging of atoms and molecules particularly movement of electrons called magnetism. The mechanism of magnetism is achieved by magnetic avail of substance and magnetic field is formed due to circular movement of electrons at shells of nucleus. When the current originates in metal then the magnetic field is developed, and creation of such field is termed electromagnetism. Because of rotation of electrons across nucleus and it's both rotation magnetic polarization is generated that is called magnetic dipole moments.

Mathematically magnetic dipole moments are given by equation

$M = \mu \text{ total}/$ (1.1)

Where

M = magnetic dipole moment, V = volume

μ total = total (net) magnetic dipole moments

Magnetic induction B magnetic field solidity of magnetic substance is given by

$$B = B_0 + \mu_0 M \quad (1.2)$$

Where,

B_0 is an external applied magnet field

We refer to the magnetic permeability of free space as $\mu_0 = 4\pi \times 10^{-7}\ WbA^{-1}m^{-1}$.

The magnetic material's field strength H, expressed in terms of M and B, is determined by

$$H = B/\mu_0 - M \quad (1.3)$$

And

$$B = \mu_0 (M + H) \quad (1.4)$$

Where M and H both have the same unit

$$B = \mu_0 \mu_r H \quad (1.5)$$

Where,

$$\mu_r = (1 + M/H) \quad (1.6)$$

1.3 Magnetic Material Types

Materials with indications of magnetism and magnetic properties come in a variety of forms.

- Diamagnetic materials
- Paramagnetic materials
- Ferromagnetic materials
- Antiferromagnetic materials
- Ferrimagnetic materials

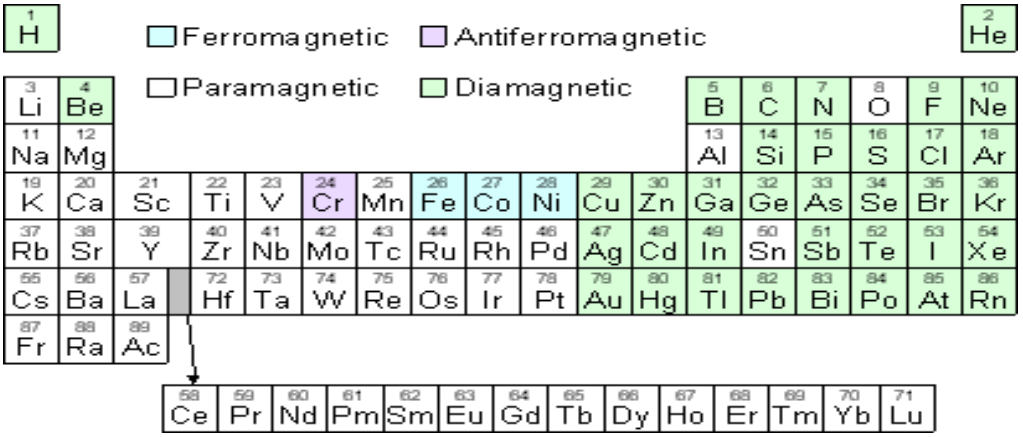

Figure 1.2: Periodic table with magnetic arrangement of materials.

1.3.1 Diamagnetism

Diamagnetic materials have too slight magnets in immediacy of extraneous magnet field and have poor repulsion while magnet field is involved. Magnetic fields generated in this group oppose the foreign magnetic fields. Diamagnetic materials unflavored magnetization [9]. Diamagnetism is followed by those attires having paired electrons and these equipment's have negative and little susceptibility of range 10^{-6} 10^{-3}.

In diamagnetic substances electronic configuration is like that all shells are absolutely filled having no unpaired electrons. Materials such as hydrogen, neon, nitrogen, helium etc. is isomagnetic in nature. Fig.1.3 shows diamagnetic materials (a) without fields (b) By applying electric fields (c) When field is removed

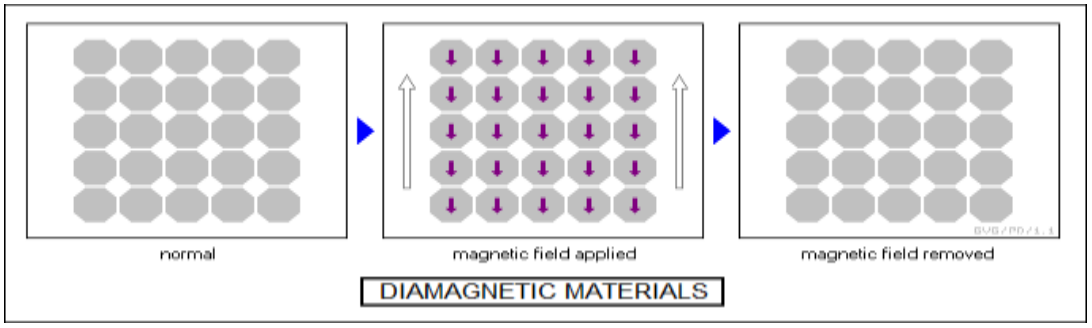

Figure 1.3: Diamagnetic materials (a) when no field is applied (b) when field is applied (C) when field is removed.

1.3.2 Paramagnetism

Materials, whichever atoms and molecules, have single electrons and have nonzero angular momentum exhibit paramagnetic features. In this kind of magnetic material,

there is no executive recission of electrons movement. Atomic moments are directed into the magnetic field when these materials are exposed to an external field otherwise, atomic moments are arranged in a disorganized form. Fig. (1.4) represents diamagnetic substances along and beyond applying field.

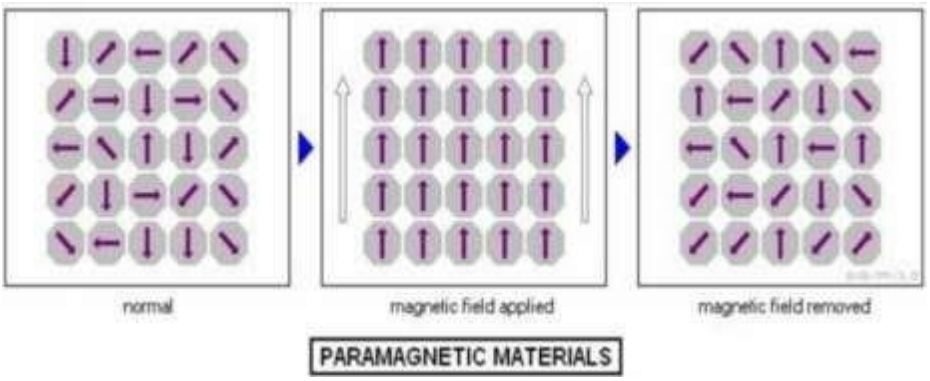

Figure 1.4**:** Materials that are paramagnetic and exhibit (a) no magnetic field and (b) a magnetic field upon application.

When external magnetic field is useful to corresponding materials, they change into magnetized materials but when external field is dislodged then they lose their magnetizations. Curie law is applicable to these sorts of materials. This law says that the correlation between magnetism and absolute temperature is inversely proportional.

$$M = C.\ B/T \qquad (1.7)$$

Where C is constant.

The direction of the applied external magnet field is the net magnetic moment. Paramagnetic materials have positive liability and value of permeability has higher than 1

In aspect of extrinsic magnet field paramagnetic substances have attractive and repulsive features like ordinary magnets [10]. The range of susceptibility is the level of 10^{-6} to 10^{-1}. When the temperature rises from above Curie temperature then ferromagnetic substances are converted to paramagnetic materials. Platinum, uranium, strontium, barium, and liquid oxygen are paramagnets substances. Fig.1.5 shows Antiferromagnetic and Ferromagnetic materials.

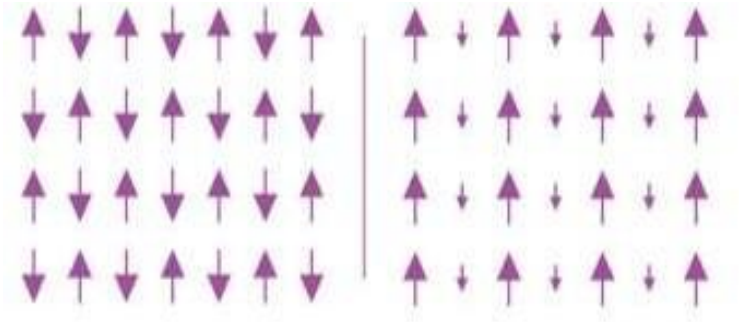

Figure 1.5: Antiferromagnetic and Ferromagnetic materials

1.3.3 Ferromagnetism

When there are no external magnetic fields present, ferromagnetic materials suddenly become magnetized, and their magnetic moments are ordered in a parallel way [11]. Due to superimposed wave positions of atomic and ionic secretiveness ferromagnetic materials brings a substitute interaction called direct exchange. There is a powerful internal magnet field in ferromagnetic substances. Spontaneous magnetization can be tolerated below a fixed temperature called Curie temperature for ferromagnetism but as temperature rises above curie temperature these substances are turned over to Paramagnetism materials. We utilize materials in daily life that are predominantly ferromagnetism such as Nickle, cobalt, and iron etc. Ferromagnetic materials like iron, cobalt and Nickle have curie temp 358 C°±5, 1131 C°±5 and 770 C°±5 respectively [12]. Fig.1.6 demonstrates ferromagnetic material (a) without a magnetic field (b) without one.

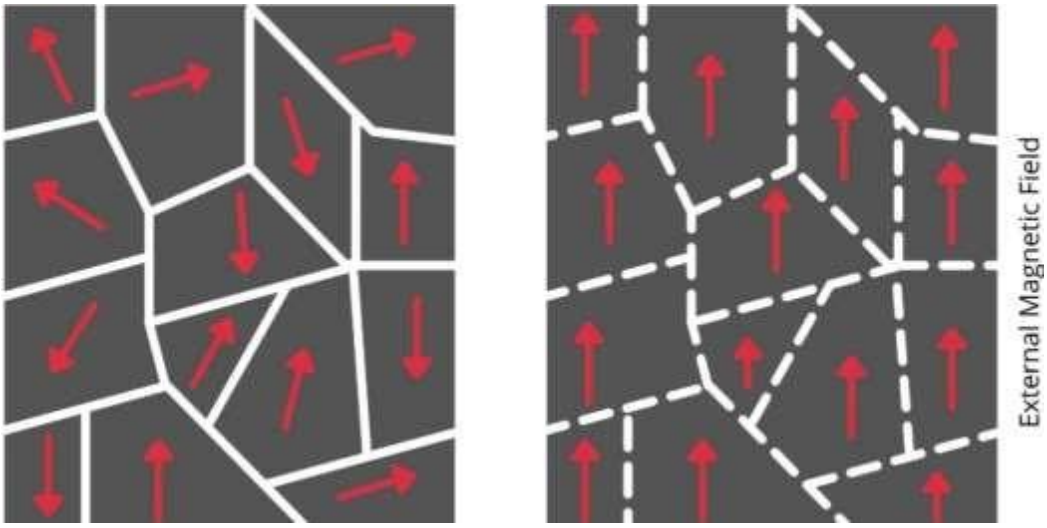

Figure 1.6: Ferromagnetism material with (a) without magnetic field (b) with magnetic field.

1.3.4 Antiferromagnetism

These are substances that have antiparallel magnetic moment arrangement without an external field. Antiferromagnetic substances are interchanged into paramagnetic substances above specific transition temperature termed Neel temperature [13]. In ferromagnetic substances there is sudden magnetization due to rotation of electrons except in case of antiferromagnetic substances there is no magnetization due to opposite rotation of electrons. This characteristic makes these materials contrary to each other. At little temperature antiferromagnetic substances have diamagnetic features. Magnetic vulnerability of antiferromagnetic materials will be largest when temperature is low set, but paramagnetic materials have elevated susceptibility with knockdown of temperature.

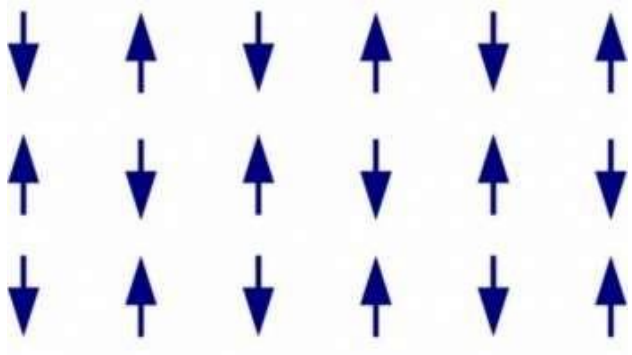

Figure 1.7**:** Antiferromagnetism material.

1.3.5 Ferrimagnetism

Ferrimagnetic substances are identical to ferromagnetic substances and magnetic occasions are anti-parallel but are not similar in magnitude. Ferrimagnetic materials show spontaneous magnetization below a certain temperature due to antiparallel alignment of magnetic moments.

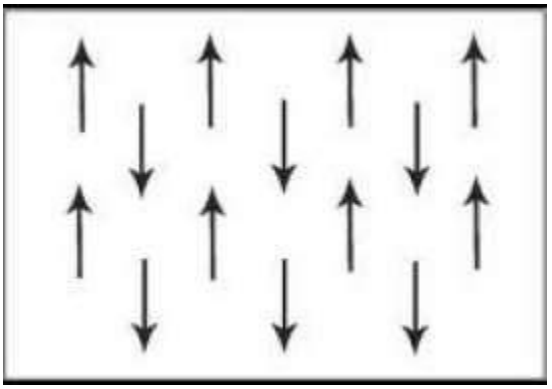

Figure 1.8: Ferrimagnetism material.

1.4 Ferrites

Ferrites are magnetic materials composed of oxides, such as ferric ions (ferromagnetic materials). The standard formula for ferrites is KFe_2O_4, where K corresponds to the divalent elements [14] comprising Fe, Co, Mn, Zn, and Ni. Zinc is also regarded as ferrite. Ferrites have strong electrical resistivity and low eddy current losses make them useful in high frequency applications. The resistivity of ferrites varies at room temperature and is influenced by chemical composition and synthesis methods. Ferrites' characteristics are influenced by several factors, including their density, homogeneity, porosity, Curie temperature, and particle size.

1.5 Categorization Of Ferrites

Ferrites come in two different forms:

- Soft ferrites
- Hard ferrites

1.5.1 Soft Ferrite

Ferrite nanoparticles have the ability to change the direction of magnetism without requiring a significant amount of energy, and soft ferrites are often ferromagnetic.

Soft ferrites have too slight coercivity and restricted area of hysteresis loop and their coercivity has ranges less than 1 KA/m. Manganese, Nickle, and Zinc ferrites are utilized in core of transformers. Due to softness in the environment due to slight coercivity they are also operated in floppy disc, switch mode power supply, video cassettes, computer memories, credit cards and computer hard disc etc [15].

1.5.2 Hard Ferrites

Hard ferrites are everlasting magnets in nature having extremely high value of coercivity and large value of remanence once exposed to magnetic zone. Hard ferrites are oxides of barium, iron, and strontium. They have a virtue of coercivity higher than 10 KA/m. Hard ferrites are utilized in various fields such as phase shifters and communication devices. Hard ferrites have the capability to give energy to protect magnetic fields for different applications. Cobalt and cobalt alloys, rare earth alloys, iron, and platinum, are predominantly hard ferrites. Hard ferrites are also employed in various fields containing telephones, generators, magnets of radio, loudspeakers, motors and in relay.

1.5.3 Types Of Ferrites

Based on the structure they have; ferrites are classified into three groups.

- Spinel ferrites
- Hexagonal ferrites
- Garnets

Zinc and its nanoparticles are part of the spinel ferrites family.

1.5.4 Spinel Ferrites

Spinel ferrites have cubical shapes having little eddy current falls and little figure of resistivity at microwave frequencies [16] and due to upward specified features they are ideal for operated. Spinel ferrites are designed by Bragg and Nishikawa in 1915. They have an ordinary formula KFe_2O_4

Here, K stands for any divalent metal ion, that are Ni^{+2}, Cd^{+2}, Mg^{+2}, Co^{+2}, Fe^{+2}, and Zn^{+2}

Spinel ferrites have an FCC configuration and a closely packed structure with the 32 oxygen ions forming a unit cell. Two interstitial positions exist, and metallic cations can occupy these sites. For divalent and trivalent iron ions, there are tetrahedral lattice sites (A) and octahedral lattice sites (B). The spinel ferrites unit cell has 32 octahedral and 64 tetrahedral lattice sites.

1.5.5 Tetrahedral Lattice Site

Interstitial molecules are crowded in the midpoint by the nearby four oxygen atoms at lattice sites. That interstitials site is famed as lattice sites (A). The fourth atom is at the top with symmetric programs, and the other three atoms are surrounded by one another in an equivalent plane. Eight tetrahedral lattice places are present in each unit cell of the FCC configuration, meaning that eight tetrahedral lattice places are engaged in addition to the 64 lattice places in spinel ferrites. Fig.1.9 demonstrates the lattice sites that are octahedral and tetrahedral.

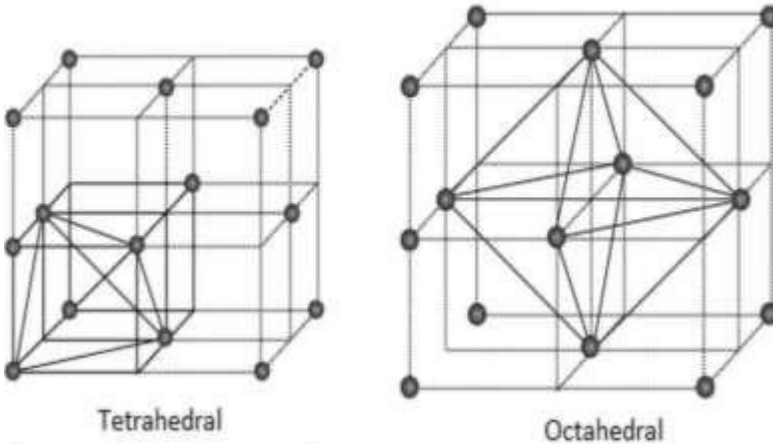

Figure 1.9: Tetrahedral and octahedral lattice sites

1.5.6 Octahedral Lattice Sites

Six neighboring oxygen atoms encircle the octahedral lattice site (B) in the spinel ferrite structure. These configurations link four atoms in a plane, with the remaining two atoms situated somewhat above and below the spinel ferrite structure. The structure of spinel ferrites consists of 32 octahedral lattice sites. The FCC unit cell's structure has four octahedral sites.

1.6 Types Of Spinel Ferrites

Depending on where the octahedral and tetrahedral lattice sites are located, there are three distinct forms of spinel ferrites.

- Normal spinel ferrites
- Mixed (intermediate) spinel ferrites
- Inverse spinel ferrites

1.6.1 Normal Spinel Ferrites

Normal spinel ferrites contain tetrahedral (A) and octahedral (B) lattice sites which include specific types of cations. Tetrahedral site (A) has divalent cations, while octahedral site (B) has trivalent cations. The metallic ions are occupied by 16 octahedral and 8 tetrahedral sites. . The formula for normal spinel ferrite is (K+2).Since k and Ke stand for divalent and trivalent ions independently, A[Ke+3]BO_4. One common form of spinel ferrites is $ZnFe_2O_3$ in bulk.

1.6.2 Inverse Spinel Ferrites

Tetrahedral sites (B) contain half of the trivalent ions in inverse spinel ferrites, whereas

octahedral sites contain the other half. Inverse spinel ferrite has the formula (Ke^{+3}) $A[K^{+2}Ke^{+3}]BO_4$ where divalent and trivalent ions are denoted by K and Ke, respectively. Fe_3O_4 is an illustration of an inverse spinel ferrite, where the Fe divalent cation is found at octahedral (B) sites [17].

1.6.3 Mixed (Intermediate) Spinel Ferrites

Because of their cationic distribution between normal and inverse spinel ferrites, Intermediate spinel ferrites are another name for mixed spinel ferrites. $(K\delta^{+2}\ Ke_{1-\delta}{}^{+3})$ A $[K_{1-\delta}^{+2}Ke_{1+\delta}^{+3}]$ B O . 4

Where the inversion parameter is denoted by δ, and K and Ke stand for divalent and trivalent lattice sites. For spinel ferrites that are normal and complete, the inversion parameter values are δ= 1 and δ = 0, respectively. Mixed spinel ferrites are defined as ferrites with an unequal cation distribution on octahedral sites [18]. Examples of intermediate (mixed) ferrites are $MnFe_2O_4$ and $MgFe_2O_4$.

1.7 Application Of Ferrites

Because of these notable and significant characteristics, ferrites are widely utilized in the engineering and technological domains [19]. Ferrites are utilized in wireless devices and electronics, such as local area networks and personal communication devices. Today ferrites are extensively utilized in medical fields in case of drug delivery for remedy of different disorders [20]. Fig. 1.10 demonstrates several kinds of materials made of ferrites.

Figure 1.10: Different types of material made of ferrites.

1.8 Zinc Ferrite Nanoparticles

Zinc Ferrite ($ZnFe_2O_4$) is a compound that combines zinc oxide (ZnO) and iron oxide (Fe_2O_3) in a specific stoichiometric ratio. It is a type of mixed metal oxide that belongs to the class of spinel ferrites, characterized by their crystal structure and magnetic properties. Zinc ferrite takes on the spinel structure, with iron ions (Fe^{3+}) occupying the octahedral sites and zinc ions (Zn^{2+}) usually occupying the tetrahedral sites. The formula $ZnFe_2O_4$ reflects a 1:2 molar ratio of zinc to iron. This arrangement results in a cubic crystal lattice with alternating layers of Zinc and iron [21].

Zinc ferrite ($ZnFe_2O_4$) has several distinctive properties, to its spinel structure and the combination of zinc and iron ions. Zinc ferrite is a ferrimagnetic material, which means it exhibits a net magnetic moment due to the antiparallel alignment of iron ions with opposite magnetic moments. However, because of the unequal distribution of magnetic moments in the material, a residual magnetization remains. Zinc ferrite exhibits moderate electrical conductivity, high resistivity, high surface area, good dielectric properties, thermal stability, restricted band gaps, high electromagnetic performance which make it an excellent competitor as an elastic magnet and low-loss energy material at peak frequencies and useful for making an efficient for various application in biomedical and energy storage devices [22].

$ZnFe_2O_4$ nanoparticles are utilized in rechargeable batteries and supercapacitors for their high surface area, excellent electrochemical performance, and ability to store and release energy efficiently, but my focus is on the study of Zinc ferrite nanoparticle, which are employed as an electrode in lithium-ion batteries to improve their conducting characteristics and function as a true component of the dielectric area for energy storage [23].

1.8.1 Coating Of SiO_2

The coating of silicon dioxide **(SiO_2)** on nanoparticles is extremely important due to the unique properties of SiO_2, which enhance the performance, stability, and functionality of the nanoparticles in various applications. SiO_2 coatings create a protective barrier around nanoparticles, preventing them from clumping together. This helps maintain the desired particle size and dispersibility in various mediums (e.g.,liquids, gases). By preventing agglomeration, SiO_2 coatings ensure uniformity in particle size, which is crucial for consistent performance in applications like drug

delivery, catalysis, and imaging. SiO_2 coatings can be tailored to control the size and shape of nanoparticles, which is critical for controlling their interactions with biological systems or other materials. The SiO_2 layer can also act as a support material that enhances the dispersion of the nanoparticles on surfaces, improving reaction efficiency and selectivity [24]. The SiO_2 coating can provide both **e**lectrostatic and steric stabilization to nanoparticles. The electrostatic interaction can arise from charged groups on the SiO_2 surface, which helps to keep nanoparticles from aggregating. Steric stabilization results from the physical barrier created by the SiO_2 layer, preventing particles from coming into close contact and forming aggregates. Coatings improve their dispersion, biocompatibility, resistance to environmental degradation, and enable surface modifications for specialized applications. This makes SiO_2-coated nanoparticles widely used in fields ranging from medicine and electronics to materials science and catalysis.

1.9 Uses Of Zinc Ferrite Nanoparticles

Due to the highly magnetic nature of Zinc ferrite nanoparticles, they are used in the field of drug delivery system, water purification, biosensor, magnetic storage devices, energy storage and magnetic resonance imaging (MRI) contrast enhancement, cancer treatment agents, and drug delivery [25].

1.10 Dielectrics

Three categories are used to classify materials: semiconductor, insulator, and conductor. Materials containing free electrons, or charges, are called conductors. Conduction bands are another feature of conductors. There is a relatively small band gap, or overlapping band gap, between the conduction and valance bands, and valance electrons are regarded as free electrons [26]. Between an insulator and a conductor, a semiconductor is significant. When compared to conductors, semiconductors have a larger energy band gap. In short, insulators are dielectric materials. These materials become polarized when exposed to an external electric field. The valance bands of insulators are fully filled, whereas the conduction bands are completely vacant. Because of the wide energy band gap, electrons cannot move around easily. When an electric field is applied, free electrons in conductor materials move in the opposite directions from field lines. Thus, the behavior of an insulator is distinct from that of conductors. Because they are resistant to materials, insulators are utilized in electrical

circuits [27,28].

Ferrites behave in the same way as insulators, which have high resistance and become stable because of their actions. The wide frequency range of microwave devices from 300 MHz to 300 GHz makes dielectric materials crucial. Ferrites are significant materials with a hard and strong chemical composition [29]. They come in a variety of sizes and are produced using various methods. Figure 1.11 illustrates the microwave spectrum.

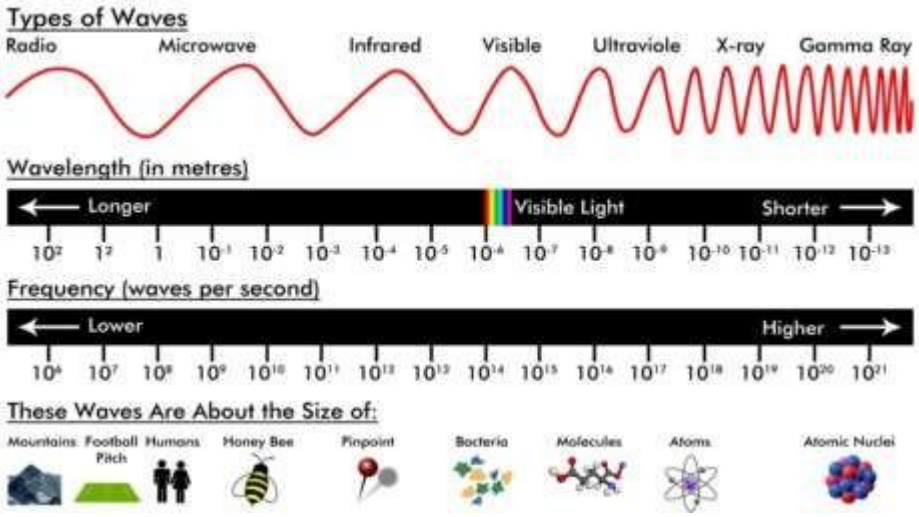

Figure 1.11: A microwave spectrum [30]

1.11 Polarization

Dipole moment per unit volume is the definition of polarization. A common method to express it numerically is

$$\boldsymbol{P} = \frac{\sum \boldsymbol{p}}{\boldsymbol{V}}$$

Ferrites can be polarized for a variety of reasons, such as electronic and atomic configuration brought on by dipole and interfacial polarization [31]. When an external magnet field is not there, polar molecules move arbitrarily; however, when a field is present, the molecules align themselves in the direction of the electric fields. Figure 1.12 illustrates that (a) polar molecules are orientated arbitrarily when there is no external electric field present, and (b) the molecules partially align with the field when one is applied.

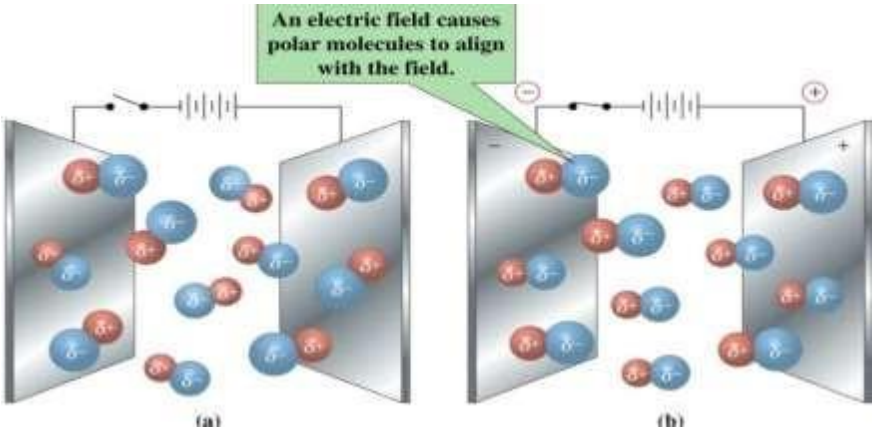

Figure 1.12.: Shows that (a) polar molecules are orientated arbitrarily when there is no external electric field present, and (b) when one is applied, the molecules partially align with the field. [32]

1.12 Types of Polarizations

There are three different types of polarizations.

1.12.1 Atomic Polarization

All electrons are confined to a particular nucleus in dielectric materials and atoms are considered a neutral entity. Although it may seem that the dielectric is unaffected by the electric field, each atom contains positive charge particles inside the nucleus and negative charge particles outside the nucleus. Consequently, the electron travels in the opposite direction from the nucleus, which moves in the direction of the electric field when external electric field is applied. Atoms are ionized by extreme fields. The force of attraction between electron and nucleus balanced in the presence of weak field which result in tiny, induced dipole.

Below figure shows small movement of nucleus toward field and movement of electrons opposite to electric field [33]. Polarizations of molecules depend upon orientation of molecules and electric field direction. In the case of symmetrical molecules, it is divided into its two components and for asymmetric molecules it depends upon polarizability tensor of fields. Fig.1.13 demonstrates slight altering of nucleus in orientation of electric fields.

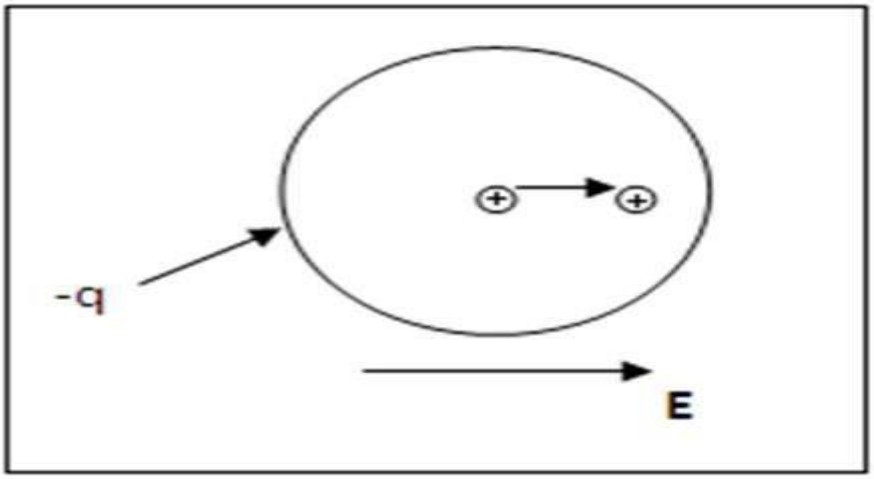

Figure 1.13: Nucleus slightly changing in the field's direction [34]

1.12.2 Dipolar Polarization

H_2O and SiO_2 and other molecules have neutral polarization. Molecules experience a torque when external field is applied due to which they become aligned in orientation of external applied field. Fig.1.14 illustrates the alignment of molecules in direction of fields when uniform electric fields are applied.

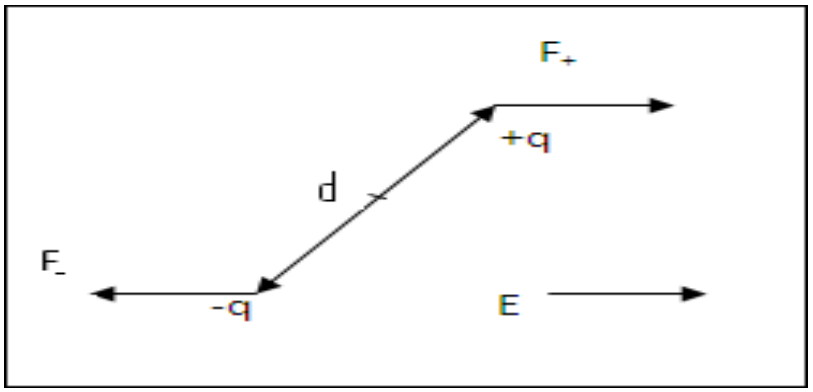

Figure 1.14: Dipole in electric field experiences a torque [35]

1.12.3 Interfacial And Electronic Polarizations

Electronic polarization is the most important polarization in the case of ferrites. The fundamental basis of interfacial polarization is Koop's theory. It is believed that molecules in interfacial polarization are composed of conducting grain borders segregated by non-conducting grain margins. The hooping mechanism will deliver electrons to the grain boundaries. Due to the considerable resistance of these grain boundaries, polarization results from the accumulation of electrons [36].

Ferrites have electronic polarization just like the conduction process in which electron

is transferred between Fe^{+2} and Fe^{+3}. Electron is displaced in direction of electric field as given below due to which polarization is produced

$Fe^{2+} \Leftrightarrow Fe^{3+} + e^{-1}$

1.12.4 Dielectric Constant

The dielectric constant, also referred to as relative permittivity, is the ratio of a capacitor's capacitance with an insulator positioned between parallel plates to its capacitance without the medium. The previously mentioned expression might be expressed numerically:

$$\epsilon' = C/C_0 \quad (1.11)$$

Were,

ε' = the dielectric constant,

C_0 = capacitance without medium, C = capacitance with medium,

The equation above can alternatively be expressed as

$$\varepsilon_r = \varepsilon / \varepsilon_0 \quad (1.12)$$

Where

ε_0 = Permittivity for the air or free the space with value 8.85×10^{-12}F/m. ε = Permittivity with medium ε_r = relative permittivity which have no dimension another way to define permittivity is in terms of the electric field and displacement vector.

Where,

D = the displacement vector

E = the Electric field

In the same way that free charges are mounted on the plates when material is positioned between them, induced bound charges are mounted on the capacitor plate when a dielectric medium is introduced, and field E is positioned between the plates. The following formula can be used to get the dielectric constant.

$$\varepsilon' = C\ d\ /\varepsilon_0 A \quad (1.13)$$

Where,

C represents the zinc ferrite pellets' capacitance, d their thickness, which may be

determined using vernier calipers, ε_0 their permittivity for empty space, and A their area, which can be computed using the formula,

$$A=\pi r^2 \quad (1.14)$$

Where, r is the pellets radius

1.13 Dielectric Loss Tangent

In the case of a capacitor, current leads voltage by 90° when no dielectric medium is added between the plates. However, when an insulator is inserted between the plates, energy is lost from the resistor or other instrument, causing a phase shift of (90°-δ) between the current and voltage. As illustrated in Fig. 1.15, the medium placed between capacitors z causes current to lead by phase shift of (90°-δ) by voltage.

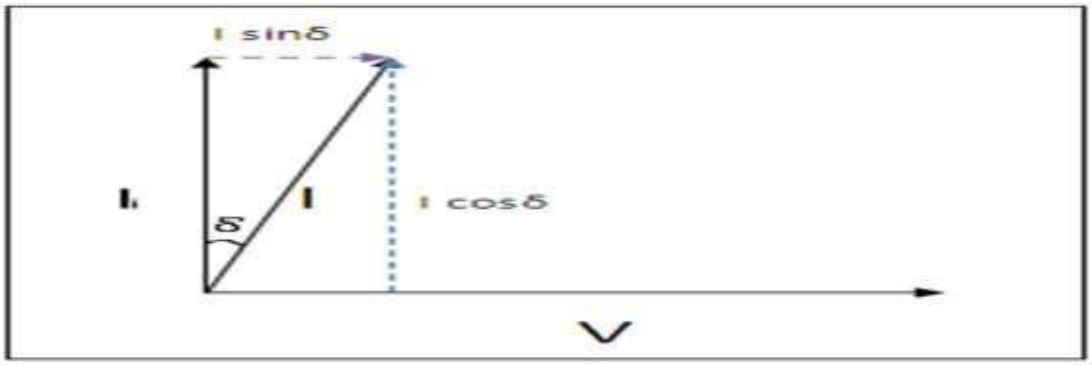

Figure 1.15: There is a slight phase shift δ in the capacitor with the dielectric material in the AC circuit, therefore the angle is (90º- δ).

Because of the little phase shift δ caused by energy dissipation in the AC circuit, the angle is (90º-δ).

$$Tan\delta = \frac{1}{2\pi fRC} \quad (1.15)$$

Where,

R is resistance, F is called frequency and C is capacitance of capacitor.

1.14 Imaginary Part of Dielectric Constant

Applying an electric field between the capacitor's plates causes the dielectric to become polarized, which causes molecules to be displaced, which enables charge to go back and forth. If oscillations are in phase, then there will be no loss in energy. In the case of dielectric molecules collide with each other and oppose each other during

oscillations results in dissipation of energy in form of heat. Material in which energy is lost by heat has dielectric constant and tangent loss; thus, dielectric loss is the term used to describe the energy loss in dielectric materials caused by an electric field. As an imaginary component, dielectric loss can be computed using the method below:

$$\varepsilon'' = \varepsilon \tan\delta \qquad (1.16)$$

All measurement readings in case of dielectric are at room temperature.

1.15 Aims and Objectives

- To Synthesize $ZnFe_2O_4$ nanoparticles.
- To control the size of nanoparticles with the help of SiO_2 coating.
- To measure the structural and dielectric properties of $ZnFe_2O_4$ nanoparticles.
- To compare the dielectric properties of $ZnFe_2O_4$ nanoparticles with SiO_2 coating.

CHAPTER 2

LITERATURE REVIEW AND SYNTHESIS

2.1 Literature Review

Ferrite nanoparticles have been nearly new in recent years in various fields due to their consequences and favorable and novel character. They are widely used in technology applications and in biomedical and engineering fields. In ferrite nanoparticles, Zinc ferrite nanoparticles have extensive use in biomedical fields and other fields. Zinc picolinate, Zinc acetate, zinc glycerate, nanoparticles have fascinated the scientists due to their various consequences of character [37,38]. In the present literature review I have engaged in consequence types of Zinc ferrite nanoparticles, Magnetic nanoparticles due to their fascinating character are ideal to utilize in various fields of biomedical such as drug delivery, magnetic resonance imaging (MRI) contrast enhancement, tissue repair, cancer treatment agents [39, 40]. Various techniques have been used for coating purposes in Zinc ferrite nanoparticles to increment the durability and functionality. Polymers and silica [41,42] are used for coating purposes in Zinc ferrite nanoparticles at a huge scale. Silica is a consequential amalgam used for coating purposes and silica is used to avoid the agglomeration of nanoparticles which increase the cohesion of these nanoparticles. Silica coating plays an important role in giving the chemically inert surface to magnetic Zinc ferrite nanoparticles in biological fields [43, 44].

Nanoparticles of nickel and cobalt were produced using the sol-gel process. The ferrite nanoparticle was calcined at the following temperatures 200°C, 400°C, 600°C, and 800°C. It was discovered that the particles had a spherical shape, great crystallinity, and a size range of 25–47 nm. It was discovered that as temperatures increased, it also increased crystalline size. As the concentration of nickels expanded, the size of nickel cobalt decreased [45]. Sol-gel produced magnesium-copper ferrite nanoparticles. By using XRD to confirm the spinel aspect, the particle size was determined to be between 17.33 and 37.34 nm. It was discovered that the average particle size dropped as magnesium adsorption increased [46]. Cobalt ferrite nanoparticles are replaced with zinc and prepared using sol-gel method. Using XRD examination, it was established that the spinel crystalline structure existed, and the particle size was (11-28 nm). It was discovered that there was an increase in zinc substitution in cobalt ferrite.

However, coercivity significantly decreased with increasing zinc concentration [47]. The sol-gel method was used to create the $MgFe_2O_4$ nanoparticles. The temperatures at which the ferrite nanoparticles were calcined were 300°C, 350°C, 400°C, and 450°C. The calcined temperature of $MgFe_2O_4$ nanoparticles affects their architectural and magnetic prospects, and the calcined temperature always boosts the lattice [48]. Using the sol-gel method, balanced cobalt-alternating copper ferrite nanoparticles were created with a particle size range of 12-32 nm. The concentration of cobalt increased because of an increase in saturation magnetization [49]. The Mn^{+2} doped cobalt ferrite nanoparticles were eventually separated by particle size into a range of 10.79 nm to 14.18 nm using the Sol-gel technique. The saturation magnetization of cobalt ferrite nanoparticles dropped as the manganese ratio was raised, yet the lattice constant only marginally increased [50]. A sol-gel approach was used to manufacture $CuZnFe_2O_4$ ferrite catalyst. Using XRD and TEM methods, the cubic crystalline structure and 10.0 nm crystal diameter were verified. The surface area of the ferrite particle falls from 95 to 41 m^2/g. Zn concentration increased, and the optical energy gap shrank from 2.25 to 1.9 eV [51]. Maghemite ultrafine particles (γ-Fe_2O_3) get ready through the Sol-Gel method with a size shorter than 5 nm. They have been prepared by using a high temperature process. Magnetic ultrafine particles have distinctive magnetic characteristics such as superparamagnetic, big coercivity, a small Curie temperature, and a captivating susceptibility boost. They have a considerable volume proportion, have sizeable surface energy, and decrease their surface energy. Naked nanoparticles have considerable chemical stability and are simple oxides in the atmosphere [52]. $MgZnFe_2O_4$ nanoparticles were processed for use as a catalyst for hydrogen production in the methanolysis of sodium borohydride. The average size of magnesium ferrite nanoparticles was found to be 10 nm. The current efficiency band gap amount was 4.77eV for $MgFe_2O_4$ nanoparticles, while the minimum amount was 2.89eV for $MgZnFe_2O_4$ nanoparticles. The $MgZnFe_2O_4$ ultrafine particles were ratified as catalysts with an elevated hydrogeneration rate of 15,957 mL min^{-1} g^{-1} **[**53]. Particles of manganese ferrite ($MnFe_2O_4$) were organized using the sol-gel auto-combustion technique. The symphonized nanoparticles show a saturation magnetization of 22.18 emu⁄g and a coercivity of 122.47 emu⁄g. The average crystallite size was found to be 21 nm. According to Brunner-Emmett-Teller analysis (BET), the combined nanoparticles had a width of 130.5 Å and a porosity of 0.1679 cm3⁄g [54]. Using the sol-gel method, Mn-Mg-Co ferrite ultrafine particles were

symphonized**.** . A cubic-shaped nanoparticle with an average size of 32 nm was identified. Magnetic measurements revealed nearly ferrimagnetic behavior, with a saturation magnetization of 38.90 emu/g at ambient temperature. These results strongly support the potential use of $MnMgCoFe_2O_4$ nanoparticles as a potential treatment for magnetic-mediated hyperthermia in a variety of applications [55]. The cobalt and holmium-co-doped nickel ferrite ultrafine particle and naked nickel ferrite ($NiFe_2O_4$) nanoparticles were harmonized by the wet-chemical method. The structural, morphological, and light intake characteristics were investigated for adopting a well-known physical, electronic, electronic and optical technique. The co-doped ferrite photocatalyst's tuned structural character makes it capable of absorbing maximal wavelengths from the UV and visible regions, and the optical band gap is 1.73eV. These doped ferrites display excellent photocatalytic activity, making them feasible for environmental remedy application in textile industrial applications [56]. The pure and co-doped multiferroic bismuth ferrite (BFO) ultrafine particles were harmonized by the sol-gel technique, and the average particle size was found to be reduced from 66 to 23 nm. The maximal polarization and remanent magnetization highly increment to 12.5 and 7.5μC cm^2, respectively, in $BiSmFeCoO_3$. The gain in conduction and lower resistance of co-doped sampling may also be suitable for a photoelectric solar cell [57]. The $CoFe_2O_4$ ultrafine particles were successfully synthesized by using the gamma-radiation method, and the particle size was found to be shorter than 10 nm. The magnetic evaluation shows that the ultrafine particles have a superparamagnetic character above 300K with a small coercivity (HC= 0.9) and a very huge magnetization nearest to 70 Am_2Kg^{-1} [58]. Lithium-doped magnesium ferrite was amalgamated by employing the Sol-gel technique. The nanoparticles were formed at 950Cº, and XRD corroborates the cubic shape of the sample. The crystallinity of the sample was also in the small range, and the lattice constantly initially got larger with dopant absorption and then decreased. The increase in conductivity and better solidity of the sample makes them potential for climate, industrial, and numerous other biomedical operations [59]**.** The fusion of pure and bi-doped nickel cobalt ferrite nanoparticles was described by employing the solution combustion route pursued through calcination at 600Cº. The average particle size was found to be 17-22 nm, and saturation magnetization, coercivity, and squareness ratio were found to be at their maximum. The huge coercivity (HC = 916.8Oe) indicates the hard ferromagnetic behavior of the sample [60]. Copper-ferrite $CuFe_2O_4$ nanoparticles

were prepared through the sol-gel technique. The ferrite nanoparticles were calcined at different temperatures (200 ºC, 450 ºC, 650 ºC, and 850º C). The ordinary particle size was constituted to be in the domain of 26–43 nm. Coercivity was 517.16 $emug^{-1}$, residual magnetization was 11.64 $emug^{-1}$, and saturation magnetization was 32 $emug^{-1}$ As AC conductivity rises, the imaginary portion of the dielectric constant rises in frequency.

2.2 Synthesis Of Ferrite Nanoparticles

Ferrite and zinc ferrite nanoparticles can be made in a variety of ways. Since size, form, and other parameters can be controlled in a variety of ways, each approach has its own restrictions, boundaries, benefits, and drawbacks. Ferrite and zinc ferrite nanoparticles can be synthesized using two primary methods and numerous secondary techniques.

2.2.1 Chemical Methods

- Chemical vapor deposition
- Micro emulsion techniques
- Chemical techniques
- Sonochemical techniques
- Wet chemical process
- Co-precipitation method
- Hydrothermal synthesis
- Vapor phase synthesis
- Sol-gel process

2.2.2 Physical Methods

- Sputtering
- Inert gas condensation
- Laser ablation
- Spray route pyrolysis

2.3 Synthesis Of Zinc Ferrite Nanoparticles Embedded In SiO_2

There are various forms of Zinc ferrite nanoparticles e.g. Zinc picolinate, Zinc acetate, Zinc glycerate. Our interest was in preparing Zinc ferrite nanoparticles especially due to their diamagnetic nature and use in lithium-ion batteries, super-capacitor and bio-medical applications. Since interparticle magnetic interactions can affect particle size and other properties, we utilize a silica matrix to control these properties. Our technique for synthesis these zinc ferrite nanoparticles embedded in the silica matrix. This process is a chemical process called the sol-gel method. Zinc ferrite nanoparticles were synthesized using various chemicals like ethanol, citric acid ($C_6H_8O_7.H_2O$) with 99% purity, zinc nitrate ($Zn(NO_3)_2.6H_2O$) and iron nitrate ($Fe(NO_3)_2.9H_2O$) with purity over 99% with help of different steps given below.

- Zinc ferrite nanoparticles/SiO_2 (0 wt. % of total nitrates, also known as bare or pure nanoparticles)
- Zinc ferrite nanoparticles/SiO_2 (5 wt. % of total nitrates)
- Zinc ferrite nanoparticles/SiO_2 (10 wt. % of total nitrates)
- Zinc ferrite nanoparticles/SiO_2 (15 wt. % of total nitrates)
- Zinc ferrite nanoparticles/ SiO_2 (20 wt. % of total nitrates)

These samples required an annealing temperature of 900 °C. The ground sample in powder form before annealing is shown in Fig. 2.1.

Figure 2.1**:** Powder form of Zinc ferrite nanoparticles before annealing

All chemicals in appropriate ratios as measured by physical balance are mixed in beakers and synthesized two steps sol-gel methods. Take 10 grams of iron nitrate (Fe

$(NO_3)_2.9H_2O$) and 3.70 grams of zinc nitrate in one beaker with an addition of 20 ml of ethanol. I placed this beaker on a magnetic stirrer for continuously stirring. I took approximately 7.15g of citric acid ($C_6H_8O_7.H_2O$) and mixed it with 20 ml of distilled water in the second beaker. This beaker is placed on another beaker for continuous stirring to get homogeneous mixture. After a few minutes of homogeneous mixing, this solution is poured drop by drop in beaker of main solution (Iron nitrate and zinc nitrate solution). This main solution is again placed on a magnetic stirrer for homogenous and uniform solution. After a few minutes of continuous stirring, pH is checked and found to be zero. Ammonia is then added to the solution until the pH becomes 9. A few minutes later, appropriate ratios of TEOS (Tetra ethyl orthosilicate) and water are added drop wise for coating purposes. Heat at 80 ºC is given to the beaker with continuous stirring on magnetic stirrer till the formation of gel. I removed the beaker from magnetic stirrer and placed in microwave oven at 100 ºC for overnight (18 hours) to dry this gel. The sample is removed from oven and ground it in mortar and pestle and placed in chamber furnace for four hours at 900 °C for annealing purpose. The sample is removed after cooling purpose from chamber furnace and ground this sample again to get desired nanoparticles $ZnFe_2O_4/(SiO_2)_y$ with y= 0, 5 wt.%, 10 wt.%, 15 wt.% and 20 wt.%. For pure or bare nanoparticles (0 wt. % sample has no addition of TEOS and water). For samples of 5 wt. % a quantity 0.6 ml of TEOS and 0.20 ml of water are added in solution respectively. For samples of 10 wt. % a quantity of 1.2 ml of TEOS and 0.40 ml of water are added in the main solution respectively. For sample of 15 wt. % a quantity 1.8 ml of TEOS and 0.60 ml of water are added in main solution respectively in the case of 15% sample amount of TEOS and water of 1.8 ml and 0.6 ml are added respectively. For samples of 20 wt. % a quantity of 2.40 ml of TEOS and 0.80 ml of water are added in the main solution respectively. These samples are ready for different measurements to check the effects of coating on various parameters of these nanoparticles.

2.3.1 Synthesis Equation

$Zn+2H_2O$----------$Zn(OH)_2+H_2$ (i)

$Zn(OH)_2$----------$ZnO+H_2O$ (ii)

$4Fe+3O_2$----------$2Fe_2O_3$ (iii)

Fe_2O_3+ZnO---------$ZnFe_2O_4$ (IV)

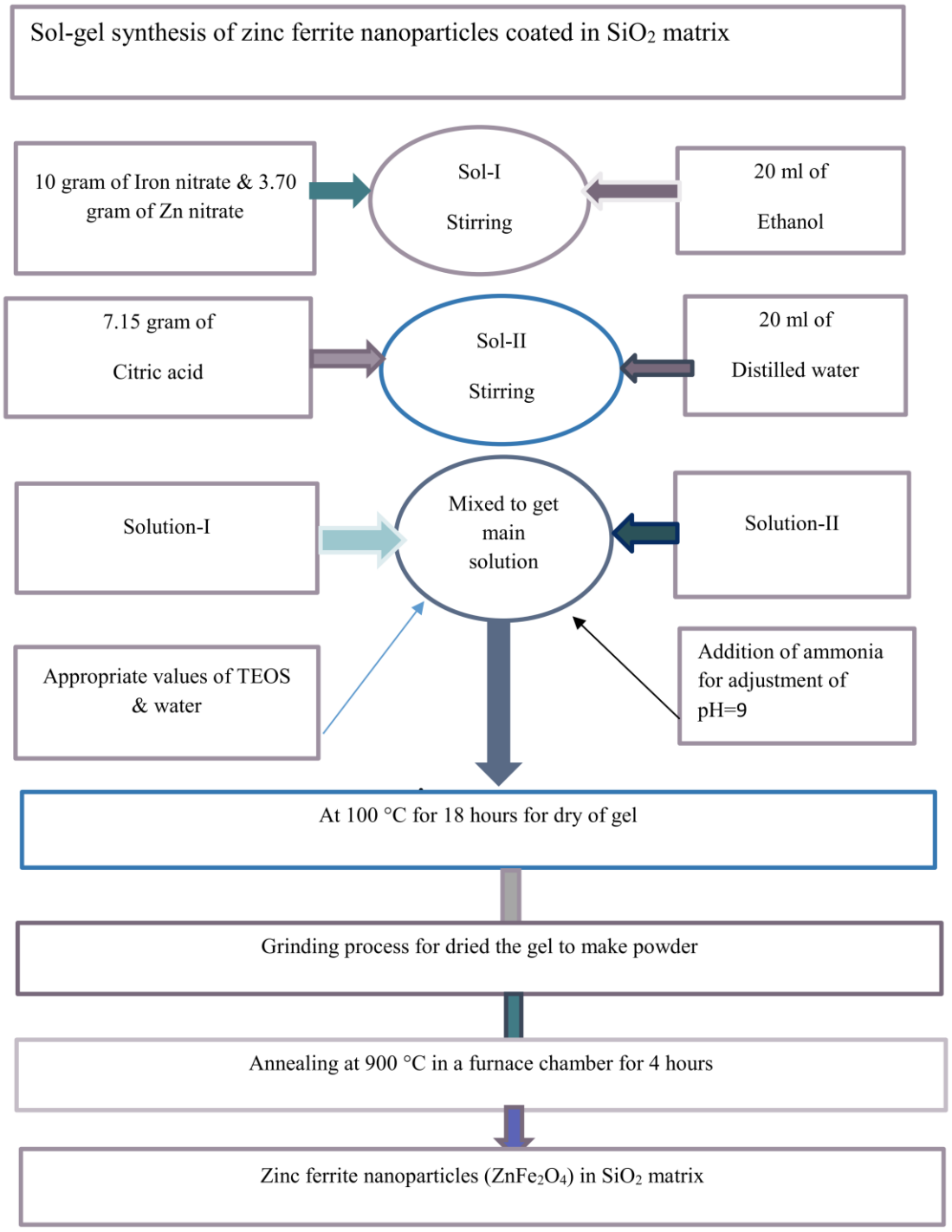

Figure 2.2: Flow chart for synthesis process of zinc ferrite nanoparticles coated in SiO_2 matrix

CHAPTER 3

EXPERIMENTAL TECHNIQUE

Many experimental techniques are utilized to examine the ferrite nanoparticles. We can obtain information about internal geometry, bonding, physical and chemical characteristics and for examination of structure. In recent work various techniques were utilized for study of zinc ferrite nanoparticles.

3.1 Crystal Diffraction

All materials have building blocks, termed lattice. In crystals there is systematic and periodic configuration of lattice. There are two or three horizons in lattice structure. Lattice has three interfacial aspects and interatomic spacings as displayed in the diagram below. In the diffraction process XRD peaks are gained due to regular and repeated designs of lattice. Fig.3.1 demonstrate geometrical figure of lattice with angles and lengths

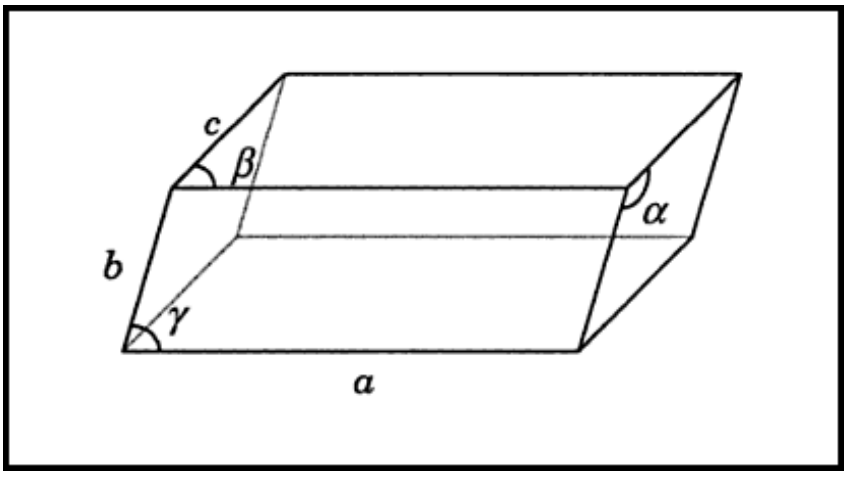

Figure 3.1: Lattice geometric shape with lengths and angles [61]

Crystal diffraction is a technique that is used to get sequences of atoms and molecules in crystal structure. By utilizing beams of X-rays of definite wavelength which falls and dissipated back to provide information about arrangement of crystals. This beam provides facts regarding bonding and other parameters of crystals. Diffraction methodology is operated to obtain information around both the temperament of material that is crystals and amorphous. Crystalline substances may be in the shape of semiconductors, conductors organic or inorganic nature. We can determine the size of particles, bonds length and atomic spacing by utilizing crystallographic techniques.

Diffraction techniques are also utilized to investigate the structure of DNA, proteins, and vitamins. For productions of diffraction there are various methods that are present such as neutron diffraction, X-rays diffraction, and electron beam splitter. Atoms are in 3-dimensional arrangements having distance d among these atoms and this spacing is termed slit in crystal structure. To create diffraction in crystal light be directed of the arrangement of length uniting these molecules otherwise it is hard to produce diffraction.

3.2 X-Ray Diffraction (XRD)

X-rays, diffraction produces when electrons are emitted from inner shells. X-rays are the released photons produced from the excitation and de-excitation of heavy atom electrons. The German scientist Roentgen made the landmark discovery of X-rays, although the nature of these rays was unknown at the time of discovery, therefore the name X-rays are formally termed processes that provide information about the nature of crystallography, bonding configurations and arrangements of any material, lattice structure, directions of crystal growth, and grain width and crystal deformities. The X-ray diffraction technique is widely used for quantifying nanoparticles and inflating the structure of materials.

3.2.1 X-Rays Production

As seen in Fig. 3.2, Filament F releases negative particles thermodynamically as an electron beam collides with a heavy material like tungsten.

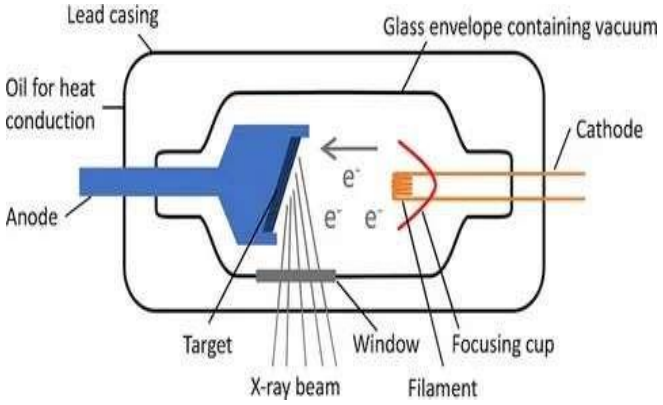

Figure 3.2**:** cooling tube for X-rays [62]

To achieve that goal, cooling tubes are used. X-rays possess an electromagnet nature because their wavenumber ranges from 0.5 A° to 2.5 A°. This wavenumber range corresponds to the wavelength of hard materials [63]. X-ray diffractometer with a

Bragg-law foundation.

3.2.2 Bragg's Law

Bragg's Law is a fundamental principle that describes the relationship between the angle at which X-rays (or any other waves) are diffracted by the planes of atoms in a crystalline material and the spacing between those planes. The law was created in 1913 and was designated for the British physicists William Lawrence Bragg and his father, William Henry Bragg. The law provides a condition for constructive interference of waves diffracted by the crystal planes, meaning that the diffracted waves strengthen each other when their path difference is an integer multiple of the wavelength of the incident wave.

The equation for Bragg's Law is:

$$2d\sin\theta = n\lambda \qquad (3.1)$$

1, 2, 3... = fringe ordering nλ = the X-ray beam's wavenumber d = the distance between two planes, θ = angle among plane and beam of light

Experimental arrangement of Bragg's Law as demonstrated in Fig. 3.3

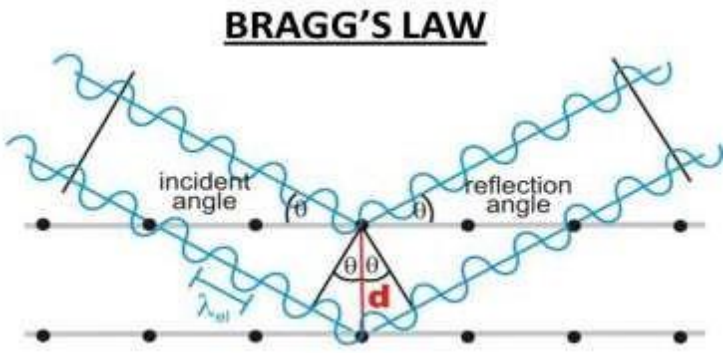

Figure 3.3**:** Arrangement of the Bragg Law in experiment [64]

The following formula can be used to measure the lattice specification quantity for cubical spinel composition.

$$a = d/\sqrt{(h^2 + k^2 + l^2)} \qquad (3.2)$$

Where the miller indices are denoted by h, k, and l. By applying the knowledge from XRD, several properties can be assessed. X-rays with wavelengths ranging from 0.6 A° to 1.9 A° are typically used in experiments. Various techniques are used with this

goal in mind.

- Powder method
- Laue method
- Rotating crystal method

3.3 Powder Method

The powder procedure is utilized to investigate the crystal structure. A large amount of crystalline material is present in different types of powder; θ changes only when powder is used in conjunction with rotating crystal process. The arrangement of the crystal is altered when X-ray beams pass over the powder, as shown in Fig.3.4 Powdered Crystal Spectrometer.

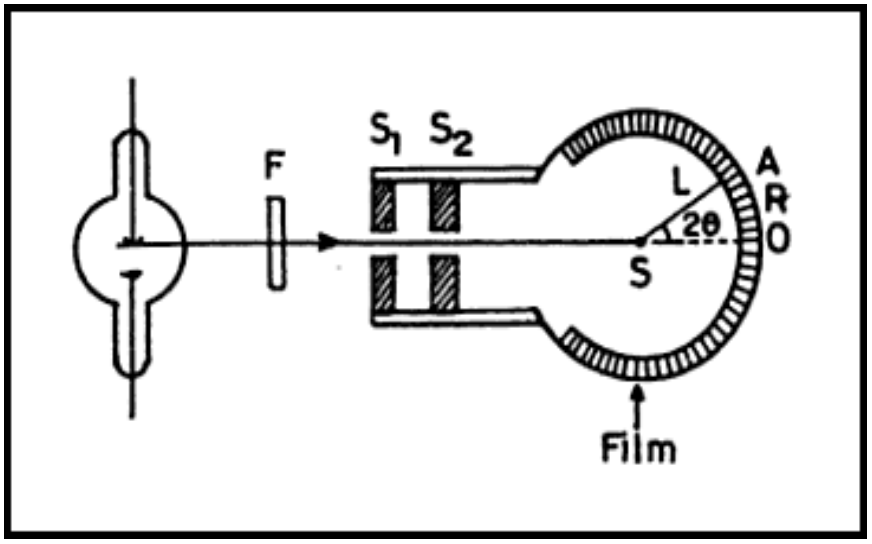

Figure 3.4: Powdered crystal spectrometer [65]

In this instance, θ varies noticeably as different wavelengths of light surround the powder; yet diffraction primarily occurs at wavelengths that satisfy Bragg's law.

3.3.1 Laue Method

This significant technique determines the orientation and nature of the material, i.e., whether it is a single crystal or polycrystalline material [66]. Laue made the discovery in 1912. This approach has a wavelength λ that fluctuates and a constant δ. All wavelengths of radiation are employed in the investigation of crystal structure. The photographic film is captured with a Laue camera. The Laue method utilizes a continuous spectrum white beam. In contrast to an X-ray beam, a crystal or sample is fixed in the Laue method. This approach uses all available wavelengths, but only X-

ray beams that satisfy Brag's law provide information. The X-ray beam is diffracted and captured as a spot-on film. This film is developed after being exposed for five or six hours. The numerous spots found in developed films are referred to as Laue spots. Fig. 3.5 displays the Laue method's experimental setup.

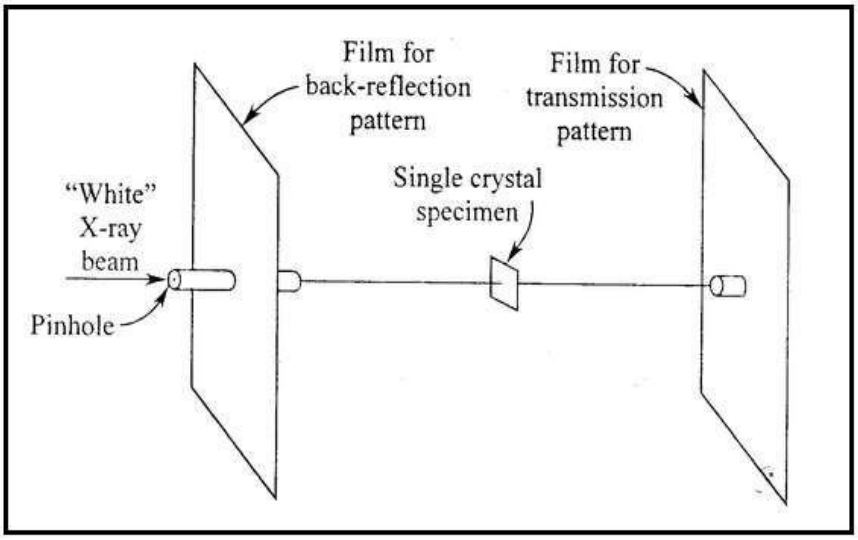

Figure 3.5**:** Laue technique experimental setup [67]

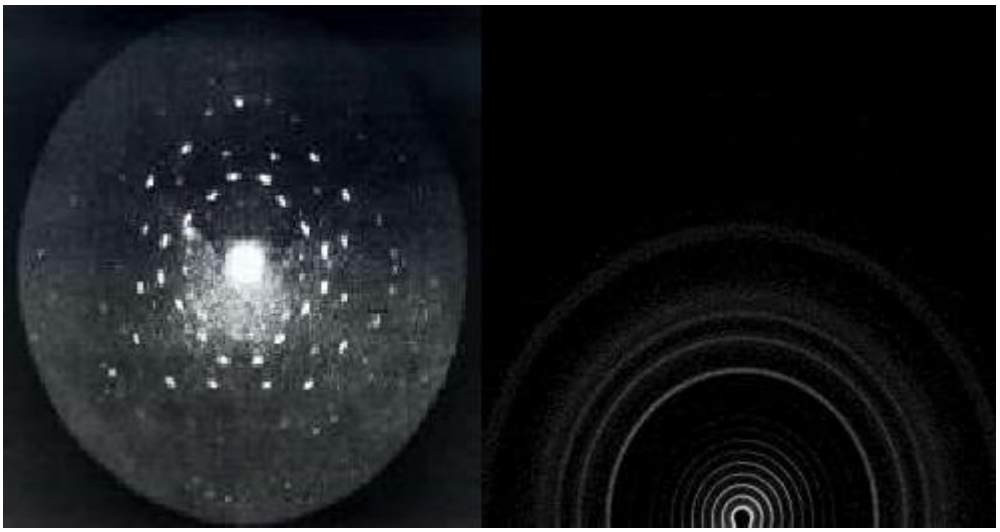

Figure 3.6: Pattern for single crystal [68]. Fig.3.7: Pattern for polycrystalline [69]

Single crystal and polycrystalline patterns used in Laue method are shown in Fig. 3.6 and Fig.3.7, sequentially

3.4 Rotating Crystal Method

This methodology was initially employed for assessment of crystal formation. This methodology is analogous to powder form and θ changes as that of powder method. samples are emplaced on spindles that have capability to rotate as demonstrated in

Fig.3.8.

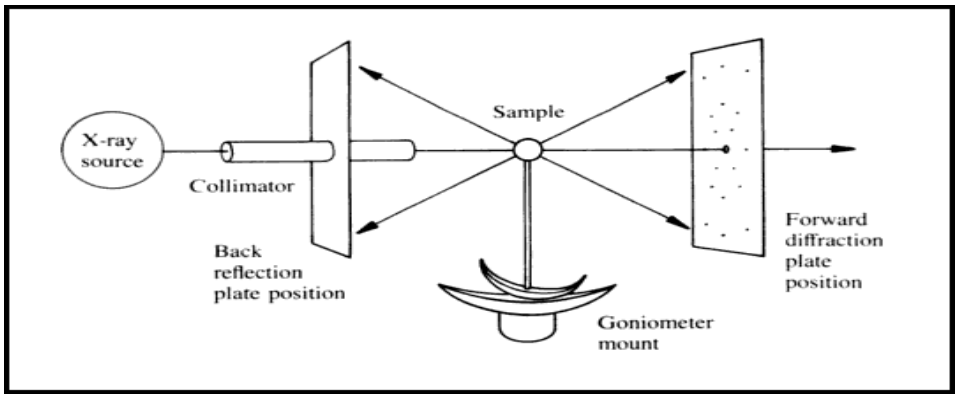

Figure 3.7: Rotating crystal method [70]

X-ray beam enters through collimator with the purpose of sampling. On photography films that are contained within a cylinder, diffraction design is obtained. The experiment continues until Bragg's law is fulfilled.

These days, a sample of materials' atoms' surface, size, and design can be ascertained using this technique.

3.5 Determinations Of Particle Size

Paul Scherer developed the Debye Scherer technique in 1918, and it is used to assess the extent of particles. The grain size range for this principle is between 0.1 and 0.2 micrometers. An optical transmission electron device can measure particles up to five percent in size. When evaluating particle diameter, the Debye Scherer equation is properly organized [71].

$$D = k \lambda / \beta \cos\theta \qquad (3.3)$$

Where

Particle size is D, dimensional small quantity K has a value of 0.91, wavelength is λ, Bragg's angle is θ, which is measured in radians, and full width at half maximum (FWHM) is β, as seen in Fig. 3.9.

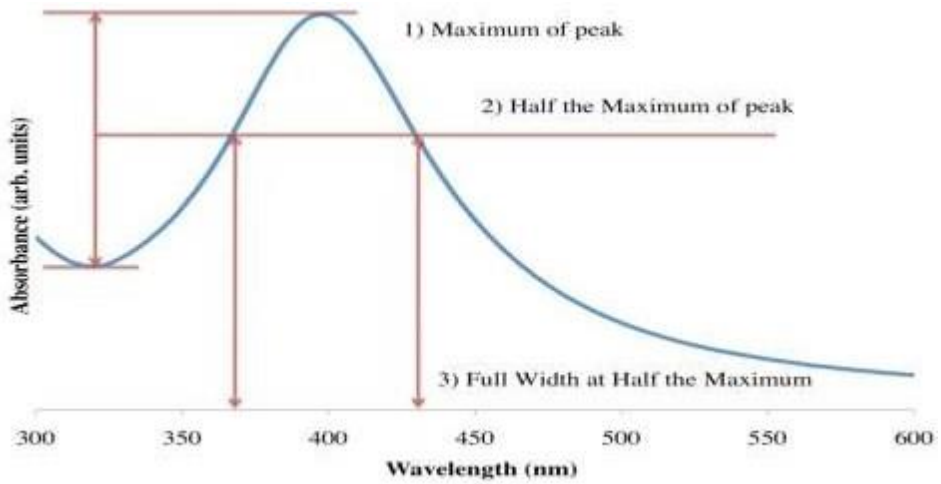

Figure 3.8: Full width at half maximum [72]

3.6 Scanning Electron Microscopy (SEM)

It is a significant scientific method for studying elements in relation to material arrangement. Grain size, particle distribution, structural framework, and material surface evaluation are all taught by scanning electron microscopy. Compared to XRD, the main advantage of scanning electron microscopy is that SEM direct images of materials.

Fig.3.10 represents image of nanocomposites taken with scanning electron microscopy (SEM).

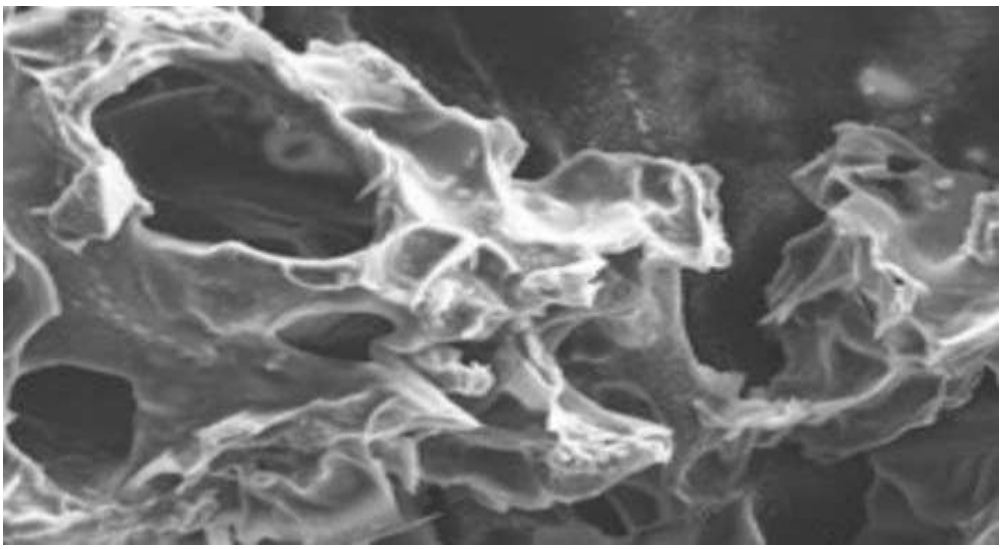

Figure 3.9: Applying a scanning electron microscope to image nanocomposites [73]

Scanning electron microscopy is comparable to optical microscopy. Electron beam is radiated hot filament or through electron channeling originator in to scanning electron

microscope. Electric field is utilized to administering the mobilization of beam of electrons, such that these electrons obtain kinetic energy and small wavelength. For accurate output the electron beam reaches a high extent of chain of electromagnetic lenses. Two kinds of microscopy are utilized for scanning electron microscopy, transmission electron microscopy (TEM) and structural analysis. Scanning electron microscopy (SEM) is applied in my current investigation trial. Scanning electron microscopy is employed to generate three-dimensional figures and unusual resolutions that are useful for investigation of substances. Beam of electrons released from sampling area and together amplified by use of detector through utilizing scanning electron microscope. Back scattered and secondary electrons provide essential knowledge about samples.

To prevent any misinterpretation in scanning electron microscopes the area of scanning electron microscope (SEM) become confirmed. Fig. 3.11 demonstrated a schematic description of SEM.

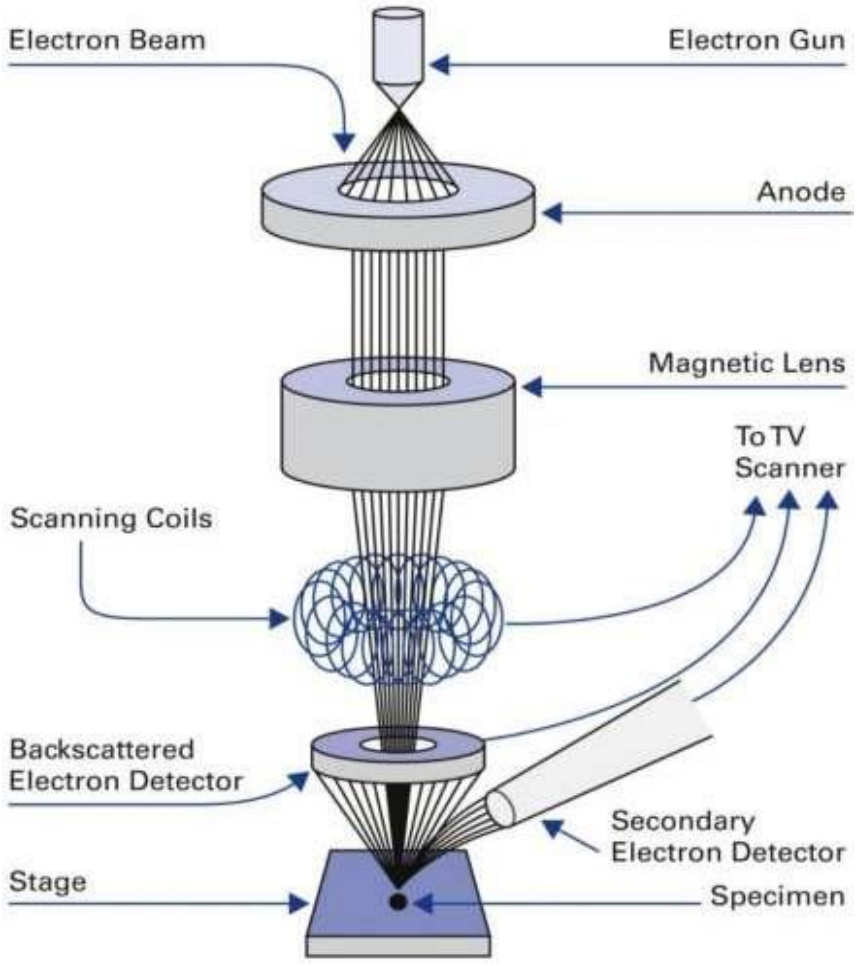

Figure 3.10: The scanning electron microscope's schematic diagram [74]

There are various troupe utilized in scanning electron microscope like hot filaments, aperture, hot filaments, an electron gun, conducting lens, and objective Lense. Electrons are released from electron guns in scanning electron microscopes and are escalated by gaining kinetic energy and exploiting high voltage 100eV to100KeV between anode and heated filament. Radiated electrons attained higher kinetic energy in scanning electron microscope that produces a diversity of wave of signals. Diffracted electrons, apparent light, backscattered electrons, heat, secondary electrons, and photons are territory of these waves of signals. Backscatter and secondary electrons are utilized for construction of specimens.

Figure 3.12 represents images by SEM with different accelerating voltages of 5 KV and 25 KV, respectively.

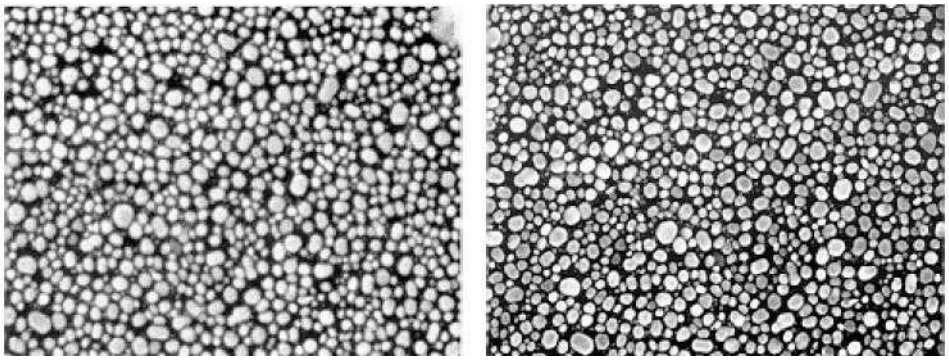

Figure 3.11: Samples of SEM (scanning electron microscope) taken at different accelerating voltages of 5KV and 25KV respectively [75]

3.7 LCR Meter

LCR meter is a significant approach that is utilized to measure the dielectric assessment of materials. It can be utilized to determine various domains like resistance, inductance, and capacitance of sample. 100 Hz to 5MHz is the LCR meter's frequency scale. There are two comparable characteristics: the dispersion and capacitance aspects—for every frequency. The automated LCR meter determines sample values in a simple way. The dielectric capacitance and dispersion characteristics that are comparable to the isolated frequency value are calculated using a single technique LCR meter. Equipment with multiple frequency modes is used to calculate different aspects by using different frequencies, such as resistance, capacitance, and inductance. The LCR meter that our lab uses at NUST for dielectric estimation is shown on Fig.3.13

Figure 3.12: LCR meter for dielectric measurement

This tool's accuracy allots the components from the bridge [76]. This data forms the basis of the LCR meter, hence leveling the bridge is necessary. The LCR meter uses an LCD (liquid crystal display) to show the sample results. The circuit description of the LCR meter bridge is shown on Fig. 3.14.

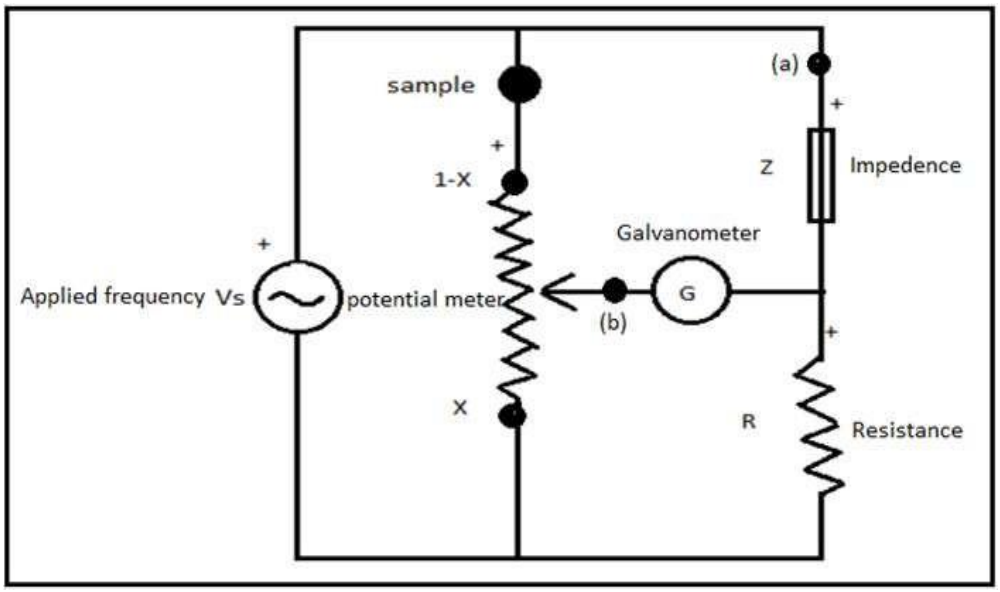

Figure 3.13**:** LCR meter bridge circuit diagram [77]

Consider an analog circuit in which a galvanometer serves as a bridge to understand how an LCR meter operates. The bridge of the LCR meter is made up of the voltage meter (potential meter) and several parts such as the resistor, capacitor, impedance, galvanometer, and sample. The LCR meter's component parts are displayed in the above figure. G, Z, R, and Rp are the components that these stands for. Rp is the potential divider meter's resistance. In instance of the LCR meter bridge, the values of

resistance R and impedance Z are acknowledged. To create quasi-balanced bridge, component parameter values are adjusted in the circuit using a potential meter. When the quasi-balancing condition is satisfied, factor P and factor Q reach their respective values. The bridge is stimulated to a constant frequency when voltage is provided to the LCR meter, resulting in reading in the galvanometer that may be positive or negative. The potential of the bridge's potential meter can be adjusted to alter the value of galvanometer. A galvanometer's value can be changed by adjusting the potential of the bridge's potential meter. Since the LCR meter's basic function is to balance the bridge, we can only determine potential values for potential meters when the galvanometer displays zero readings. When these values are obtained, the bridge is almost balanced, and P and Q values are then measured in accordance with the provided Fig. 3.15.

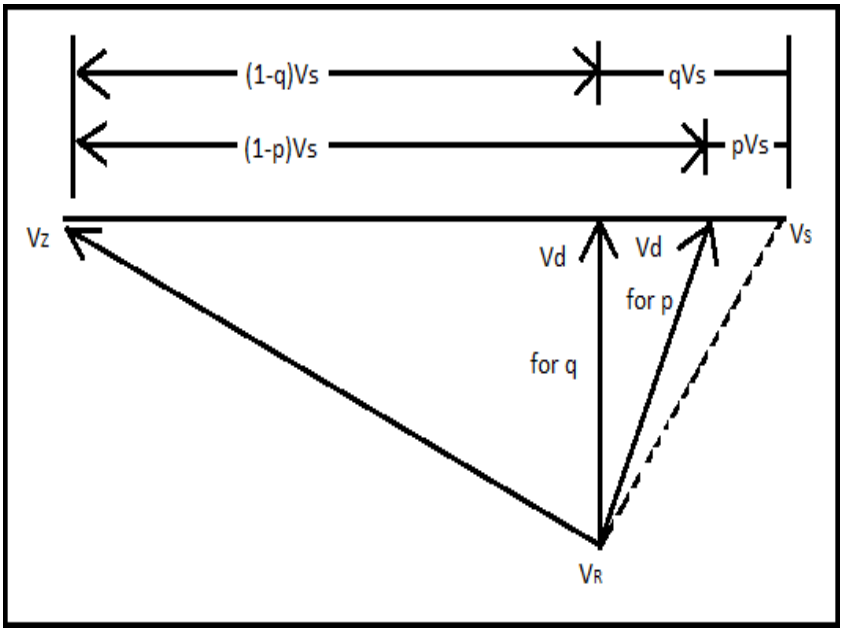

Figure 3.14**:** Phasor schematic for the LCR meter's balancing bridge [78]

Q is the point across the source and the impedance, Vd is the voltage that flows through the galvanometer at point (b), Vs is the voltage between the potential divider at point (X), and Vz is the voltage across the impedance at point (a). In a bridge, the difference between Vd and Vz establishes the first balancing point, P, whereas the difference between Vd and Vs determines the second balancing point, Q.

The following formula can be used to compute admission:

$$Y = Gp + j\omega Cp \qquad (3.4)$$

The formulas

$$Gp = p / RS (1-p) \quad (3.5)$$

and

$$\omega Cp = [1/R_S] [(q-p/1-q)^{1/2}] [1/1-p] \quad (3.6)$$

The dispersion factor or tangent loss can be determined via the following formula:

$$\tan\delta = p [q-p/1-q)^{1/2}] \quad (3.7)$$

The LCR meter's capacitance and dispersion constant can be used to compute the dielectric constant ($\mathcal{E}'_r$) and dielectric loss ($\mathcal{E}''_r$).

CHAPTER 4

RESULT AND DISCUSSION

Different types of ferrites have the potential to be used in a wide range of industries, they are promising candidates in the most cutting-edge and contemporary fields of study today. Certain parameters, such as the synthesis method, chemical synthesis, surface coating, and reaction temperature, can alter the mechanical, magnetic properties, electrical and dielectric as well as the structure of the particles on their own. Zinc ferrite nanoparticles are spinel ferrite in nature and have key role in various fields of nanotechnology. Zinc ferrites share a crystal structure with many different minerals so that oxygen, or other many elements play a crucial but interconnected role in the formation and behavior of zinc ferrite nanoparticles. The role of oxygen and iron in zinc ferrite nanoparticles is crucial for their structure, properties, and application. The cations and anions have different positions relative to each other. Zinc ferrite nanoparticles are used on a large scale in different fields of biomedicine, lithium-ion batteries.

With the Zn^{+2} ion occupying the tetrahedral sites and Fe^{+3} ion occupying the octahedral sites, zinc ferrite is referred to as a typical spinel structure. Zinc ferrite is an antiferromagnetic material with a temperature of around 10 K. Due to the magnetic quality of zinc ferrite nanoparticles, they are used in fields such as remote sensing, catalysis, storage devices, and biomedical fields such as MRI contrast agents [79] and drug delivery systems, cancer treatment agents, tissue repair, environmental remediation, sensor technology, electrochemical applications, and magnetic separation. For this purpose, we used SiO_2 as a matrix to reduce the size as well as to avoid agglomeration around zinc ferrite nanoparticles. In this work, I have prepared zinc ferrite nanoparticles coated with different concentrations of SiO_2, such as 0 wt.

%, 5 wt. %, 10 wt. %, 15 wt. %, and 20 wt. %, (y= 0 ~20 wt. %) $ZnFe_2O_4/(SiO_2)_y$} by using the sol-gel method.

4.1 X-Ray Diffraction (XRD)

Structural properties like phase purity, crystalline structure and average crystallite size of zinc ferrite nanoparticles were investigated by an important technique known as X-ray diffraction (XRD). Figure 4.1represents the XRD spectrum of bare zinc ferrite

nanoparticles with 0 wt. % to 20 wt. % of SiO_2. The obtained reflection planes (111), (220), (311), (400), (422), (333), (440), (620), (533), (622), and (444) correspond to the peaks that appeared at 2θ ranges of 18°, 30°, 35°, 43°, 53°, 57°, 62°, 71°, 74°, 75°, and 79°, respectively. These XRD peaks confirmed the cubic spinel-type structure of these nanoparticles with reference to JCPDS card No. 01-080-3537. The average crystallite size as calculated by Debye sheerer formula was found between 31nm to 63 nm. All the samples showed the single-phase cubic spinel structure, since there was no evidence of an additional phase or impurity in these peaks of particles. XRD spectrum of all these samples is represented in Fig. 4.1. As SiO_2 is in amorphous nature so that it is used to decrease the size of nanoparticles. When nanoparticles start to grow during reaction, they are used in synthesis process which blocks the energy for particle growth. The average crystallite size was calculated using the Debye-Scherer formula.

$$D=k\lambda / \beta\cos\theta \qquad (4.1)$$

Here, D represents the average crystallite size of the particle, λ denotes the wavelength of the X-ray (0.1542 nm), β represents the full width at half maximum (FWHM), K represents a dimensionless quantity of 0.91 also known as shape factor, and θ represents the Bragg's angles of the planes. The cubic spinel structure's primary (311) peak's matching lattice parameter was determined. The lattice parameters of the individual composition were determined with specific relation given below. We have also calculated the lattice parameter "a" using the relationship below:

$$a = d/\sqrt{(h^2 + k^2 + l^2)} \qquad (4.2)$$

Where

Miller indices are h, k, and l, while d is the interatomic distance between two atoms.

An increase in SiO_2 concentration is correlated with a decreasing trend in average crystallite size. Because there is many nucleation centers created during the synthesis process, an increase in silica concentration restricts the particle development and its crystallite size [80].

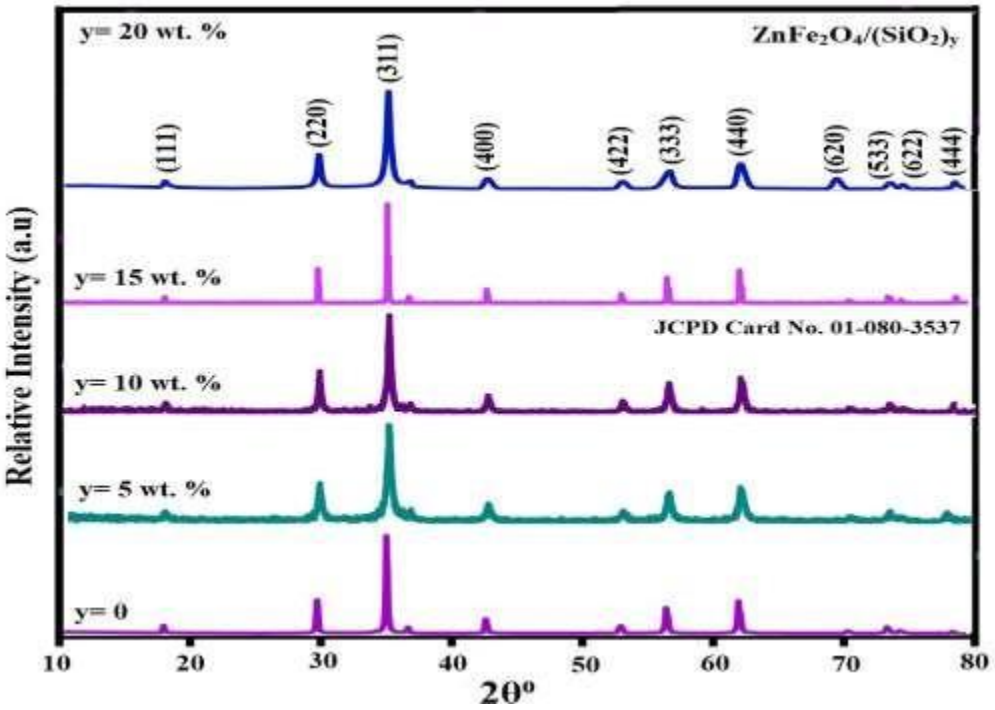

Figure 4.1: XRD pattern of $ZnFe_2O_4$ nanoparticles without SiO_2 (Pure sample) and y = 5 wt.%, 10 wt.%, 15 wt.%, and 20 wt.% respectively.

Table 4.1: Lattice parameter and crystallite size of $ZnFe_2O_4$ dispersed in SiO_2 with y = 0 ~ 20 wt %.

$ZnFe_2O_4$ nanoparticles/SiO_2(y)	Lattice Parameter (A°)	Average Crystallite size (nm)
y = 0	8.34	63
y =5 wt.%	8.36	50
y =10 wt.%	8.33	38
y = 15 wt.%	8.30	29
y = 20 wt.%	8.37	31

The lattice parameter and crystallite size were observed to decrease with increase in silica concentration due to restrictions in these parameters of nanoparticles except 20 wt. % sample of zinc ferrite nanoparticles. The sample 20 wt. % sample showed anomalous behavior due to the stresses and strains that produce the silica matrix during

synthesis of these nanoparticles as shown in Table 4.1. This behavior can also be explained by the process of agglomeration and segregation during synthesis process by silica matrix.

4.2 Scanning Electron Microscopy (SEM) And Energy Dispersive X-Rays Spectroscopy

The imaging method known as scanning electron microscopy (SEM) is used to examine the surfaces and varieties of bulk materials as well as nanomaterial. Elemental composition of zinc ferrite nanoparticles was investigated with help of energy dispersive x-rays spectroscopy. Particle size, shape, and surface structure of nanoparticles may all be estimated using SEM images [81]. SEM images and EDX spectrum of zinc ferrite nanoparticles of pure sample (y= 0 wt. %) and y= 10 wt. % and 20 wt. % are shown in Fig. 4.2 (a, a$^{/}$, b, b$^{/}$ and c, c$^{/}$ respectively). These SEM images had shown by various magnifications. These SEM images indicated the different sizes and shapes of nanoparticles such as spherical, rod and cylindrical shapes. The sample 20 wt. % SEM image indicated the agglomeration of zinc ferrite nanoparticles as results of silica matrix.

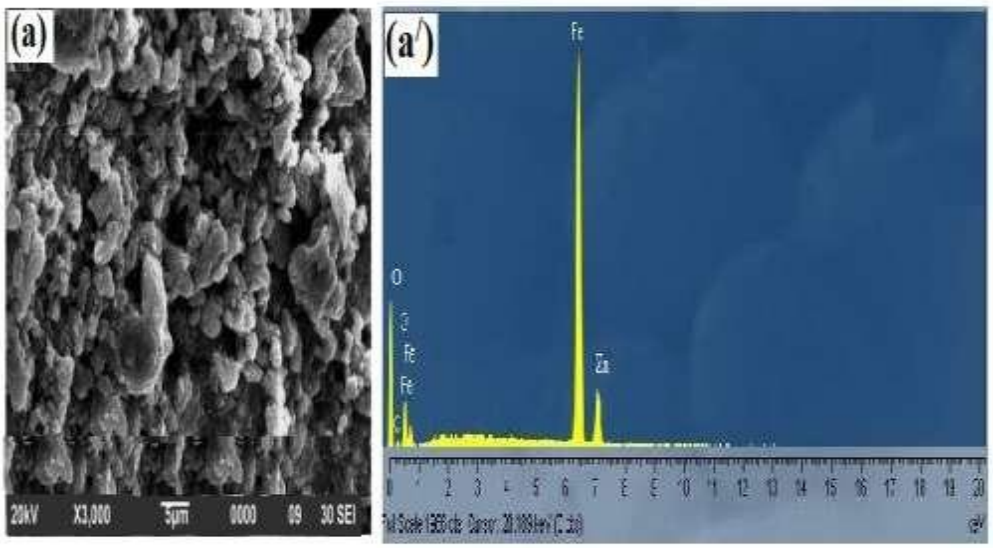

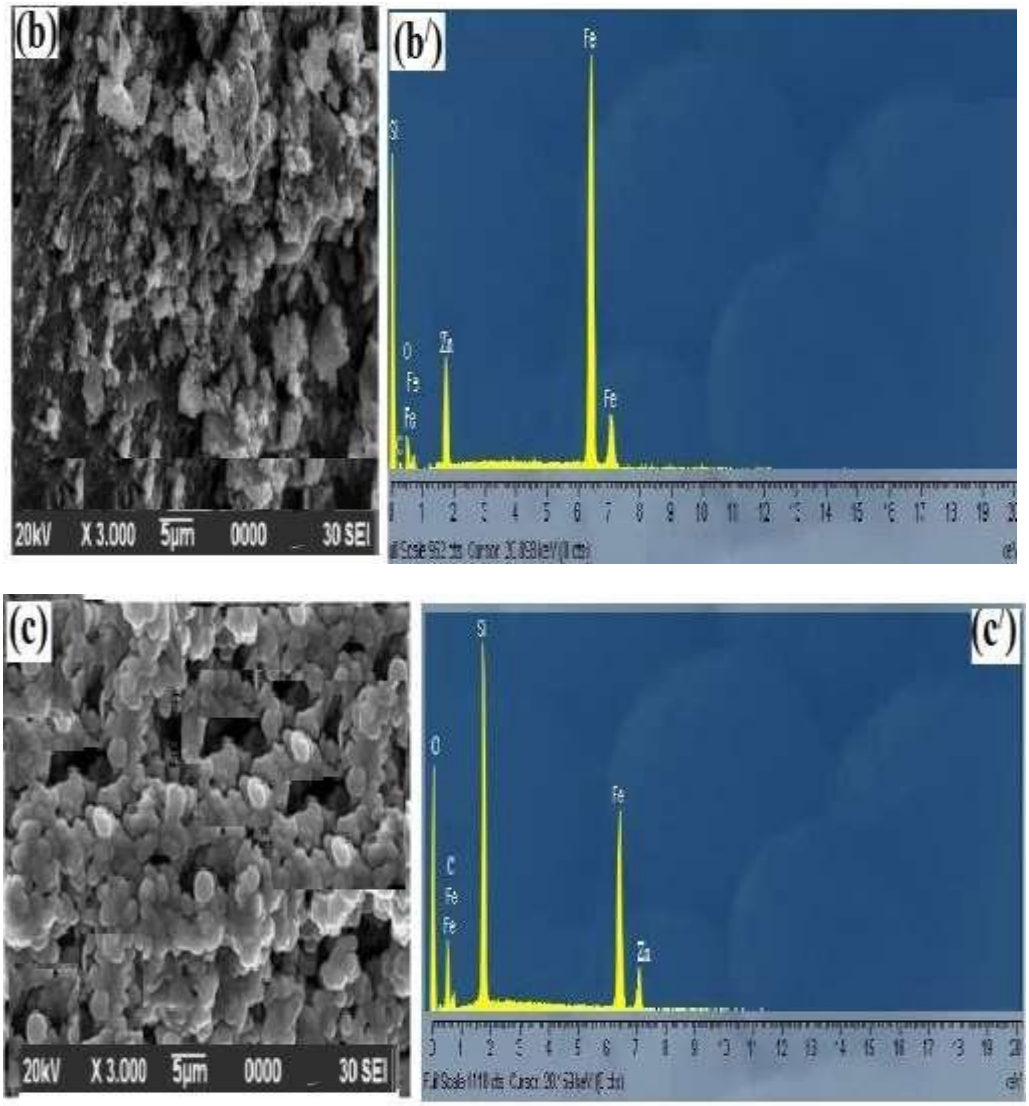

Figure 4.2: SEM image and EDX spectrum of zinc ferrite ($ZnFe_2O_4$) nanoparticles at 5µm scale and X3, 000 magnification with y= 0 (a, a/), y= 10 wt. % (b, b/) and y= 20 wt. % (c, c/) respectively.

An energy-dispersive X-ray spectroscopy (EDX) graph, sometimes referred to as an EDX spectrum, offers a graphic depiction of the sample's constituent makeup. Kilo-electron volts, or Kev, are commonly used to measure the energy of the detected X-rays, which are represented by the horizontal axis, or X-axis. Every element has distinctive emission lines for X-rays at particular energies. The intensity of X-ray counts at each energy level is displayed along the vertical axis. Different elements' distinctive X-ray emission lines are shown by distinct peaks on the graph. The EDX spectra of these nanoparticles revealed the increasing concentration of silica peaks as shown in Fig. 4,2 (a/, b/, c/).

4.3 Dielectric Properties

The dielectric properties of zinc ferrite nanoparticles coated with SiO_2 matrix were evaluated by LCR meter in frequency range of 1kHz to 10 MHz for all samples of y= 0 ~ 20 wt. % at room temperature. The dielectric properties of zinc ferrite-based nanoparticles depend on several factors, such as the ratio of Fe^{+2} to Fe^{+3} ions as well as Zn^{+2}, chemical structure, annealing temperature, and synthesis technique. Ferrites are available in a number of forms that can be used in a range of various applications, such as microwave devices, Ferro-fluid, and recording media. The dielectric properties of zinc ferrite nanoparticles coated with silica matrix were measured and analyzed in the frequency range of 1 kHz to 10 MHz at room temperature using an LCR meter. A large number of parameters such as parallel plate capacitors, real and imaginary part of dielectric constants, tangent loss and conductivity among other properties were analyzed.

4.3.1 Parallel Plate Capacitance (CP)

The dielectric mechanism of ferrites is based on different parameters, including the synthesis processes, reaction temperature, material structure, and ferrite contents. The behavior of dielectric mechanism is explained on max Wagner model as well as Koop's theory. According to Koop's theory, any material can be formed of two regions or layers. Also, any material or ferrite contain grain and grain-boundary. Grains are normally in conducting nature while grain-boundaries are normally in resistive nature. The charge carriers move from grain to grain-boundaries but when they reach grain-boundaries due to resistive nature, charges accumulate and produce hooping mechanisms and ultimately reach grain-boundaries. Max Wagner model exactly shows the similar behavior except in-homogenous medium as assumption. Parallel plate capacitance of $ZnFe_2O_4$ nanoparticles versus silica coating for all samples (y= 0 wt. % ~ 20 wt. %) was studied and analyzed in frequency range of 1kHz to 10 MHz at room temperature as shown in Fig.4.3 while Fig.4.4 indicated values of C_p versus SiO_2 coating at frequency of 1 kHz. The behavior can be explained in three regions i.e. at low frequency, at increasing frequency and at highest frequency. All samples showed that parallel capacitance was high at low frequencies, started to decrease with increasing frequency, and showed saturated values at higher frequencies. Higher frequencies cause a decrease in parallel plate capacitance because electrons lag which makes it difficult to reach the requisite region (the grain- boundary). This behavior for

$ZnFe_2O_4$ and ferrite nanoparticles is in accordance with Koop's theory and Max Wagner model [82,83]

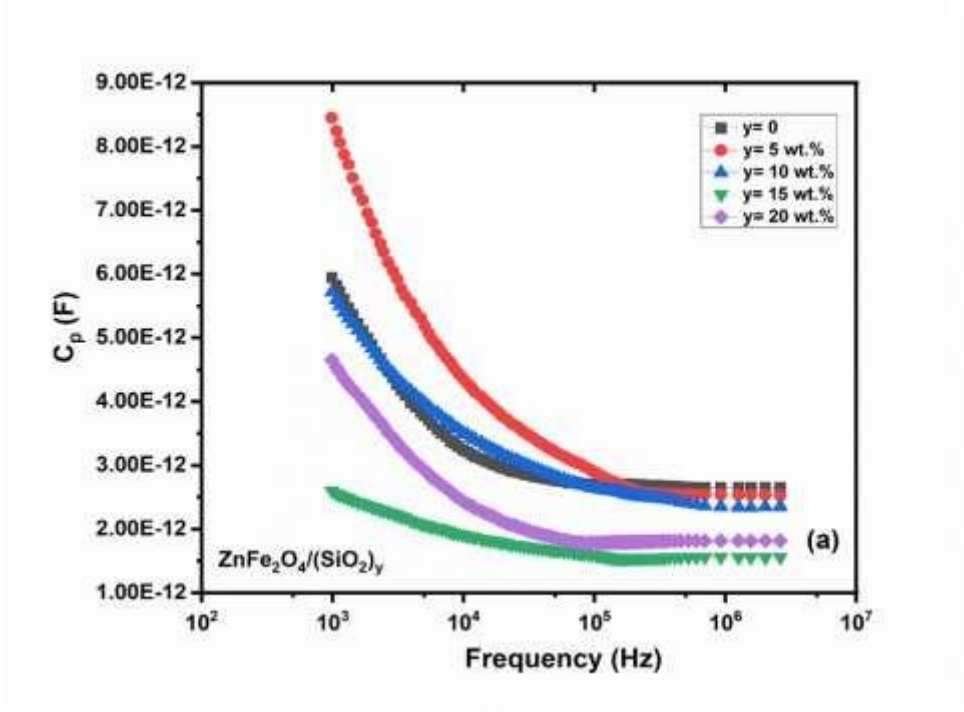

Figure 4.3 : Parallel plate capacitance (C_p) of $ZnFe_2O_4$ nanoparticles embedded with SiO_2 matrix for all samples for y = 0 wt. % ~ 20 wt. % respectively.

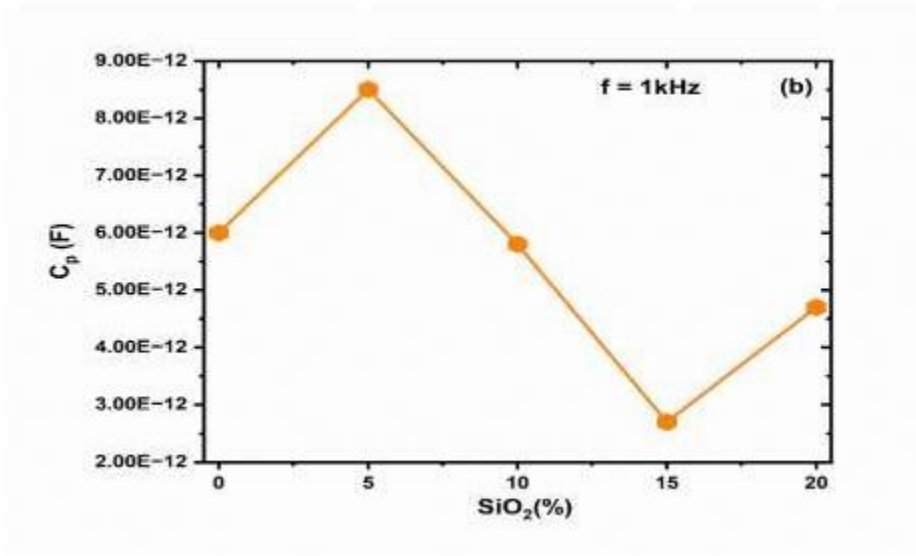

Figure 4.4: Parallel plate capacitance (C_p) of $ZnFe_2O_4$ nanoparticles versus SiO_2 matrix for all samples for y = 0 wt. % ~ 20 wt. % at frequency of 1 kHz.

The Maxwell-Wagner model, which has multiple layers but is an inhomogeneous medium, is likewise thought of as an analog of Koop's model. Due to the short time, it takes space charges to align in the direction of the electric field, electron exchange

inside Fe^{+2} and Fe^{+3} cannot follow the electric field at high frequency ranges. As frequency is raised over a certain point, the electric field reverses direction and the charge in space stops aiding in polarization, leading to constant dielectric values [84,85]. Increasing values of matrix also affects the capacitance of zinc ferrite nanoparticles. An increase in SiO_2 matrix concentration results in a decrease in crystallite size, as indicated in XRD results. The dielectric constant of material is also influenced by the reduction in particle size. Therefore, it will be interesting to analyze the dielectric characteristics of all the samples and study the effect of SiO_2 matrix concentration on dielectric properties.

4.3.2 Dielectric Loss Tangent

Dielectric loss tangent (tanδ) of dielectric materials is called the dissipation factor. The LCR meter was used to calculate the dielectric loss tangent between 1 kHz to 10 MHz The dielectric loss tangent of ferrites is dependent on a variety of parameters, including the synthesis processes, reaction temperature, material structure, and ferrite content. For ferrites, loss tangent and frequency are typically inversely related. Koop's theory and Maxwell-Wegner model can be used to explain this phenomenon. Ferrites contain two layers, according to Koop's explanation: a conducting layer that acts as the grain and a restive layer that forms the grain-boundary. Grain a second layer exhibits reciprocal behavior, whereas the first layer is more conductive and has less resistance. At low frequencies, charges accumulate in grain-boundaries with effective grain-boundaries, resulting in significant dielectric loss tangents. The tangent loss or dissipation factor of $ZnFe_2O_4$ nanoparticles versus silica coating for all samples (y= 0 wt. % ~ 20 wt. %) was studied and analyzed in frequency range of 1kHz to 10 MHz at room temperature as shown in Fig.4.5 while Fig.4.6 indicated values of Tanδ versus SiO_2 coating at frequency of 1 kHz. The dielectric loss tangent has a minimizing trend as frequency increases, which can be attributed to less effective grain-boundaries preventing charges from piling up.

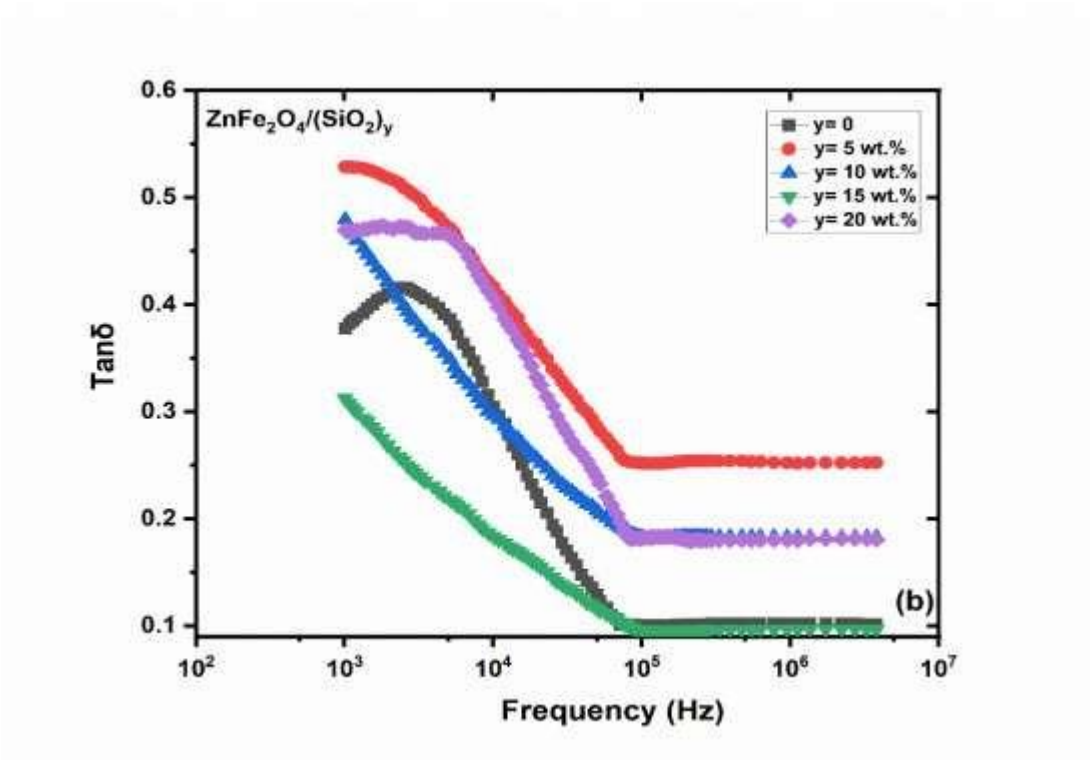

Figure 4.5: Tangent loss (Tanδ) or dissipation factors of $ZnFe_2O_4$ nanoparticles embedded with SiO_2 matrix for all samples for y = 0 wt. % ~ 20 wt. % respectively.

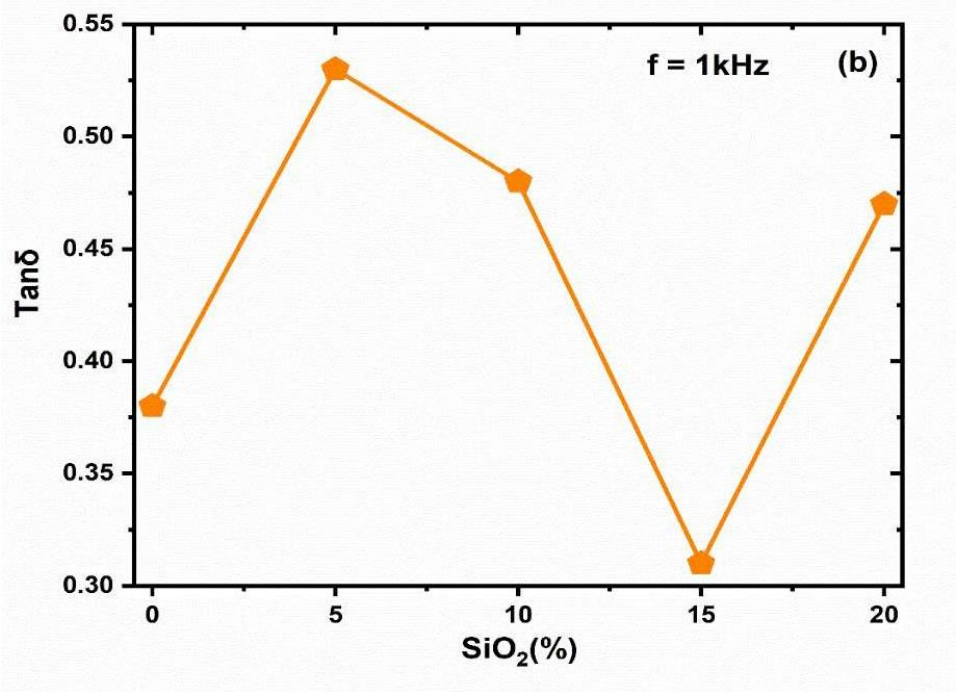

Figure 4.6: Tangent loss (Tanδ) or dissipation factors of $ZnFe_2O_4$ nanoparticles versus SiO_2 matrix for all samples for y = 0 wt. % ~ 20 wt. % at frequency of 1 kHz.

Figure 4.5 illustrates the tangent of dielectric loss as a function of frequency for all

samples of $ZnFe_2O_4$ nanoparticles that have different SiO_2 matrix concentrations. Every sample shows nearly the same trend, such as a decrease in the dielectric loss tangent at high frequencies. Dipoles become opposite to each other when they move towards electric fields, which causes the energy to be lost [86]. Also, Particle size reduces with increased SiO_2 concentration, resulting in a lesser dipole and a decrease in dielectric loss tangents. A plot between SiO_2 concentration and values of tangent loss for all samples is shown in Fig. 4.6 which indicated the anomalous behavior in samples which may be due to non-uniform distribution of these nanoparticles in zinc ferrite as resulted of agglomeration produced by silica matrix.

4.3.3 Real Part Of Dielectric Constant ($\varepsilon'r$)

The dielectric constant's real part is used to store energy in the materials. The behavior of dielectric constant may also be described based on Koop's theory and the Maxwell-Wagner model as explained in earlier section of parallel plate capacitance and tangent loss.

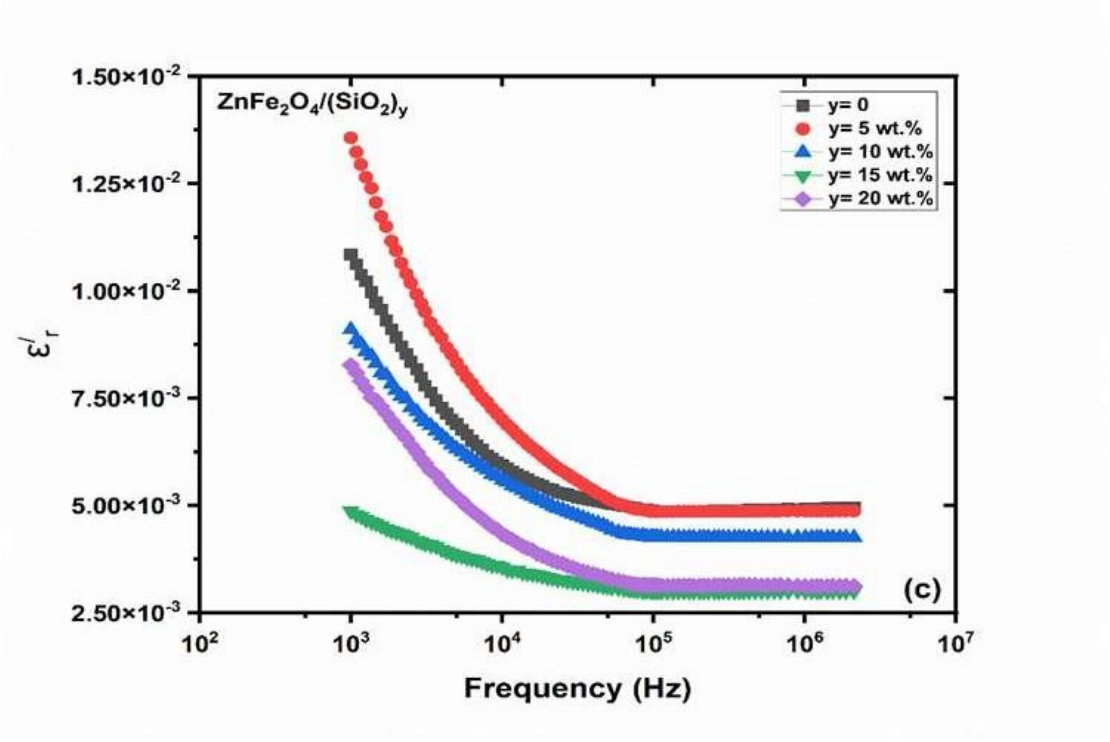

Figure 4.7: Real part of dielectric constant ($\varepsilon'r$) of $ZnFe_2O_4$ nanoparticles embedded with SiO_2 matrix for all samples for y = 0 wt. % ~ 20 wt. % respectively.

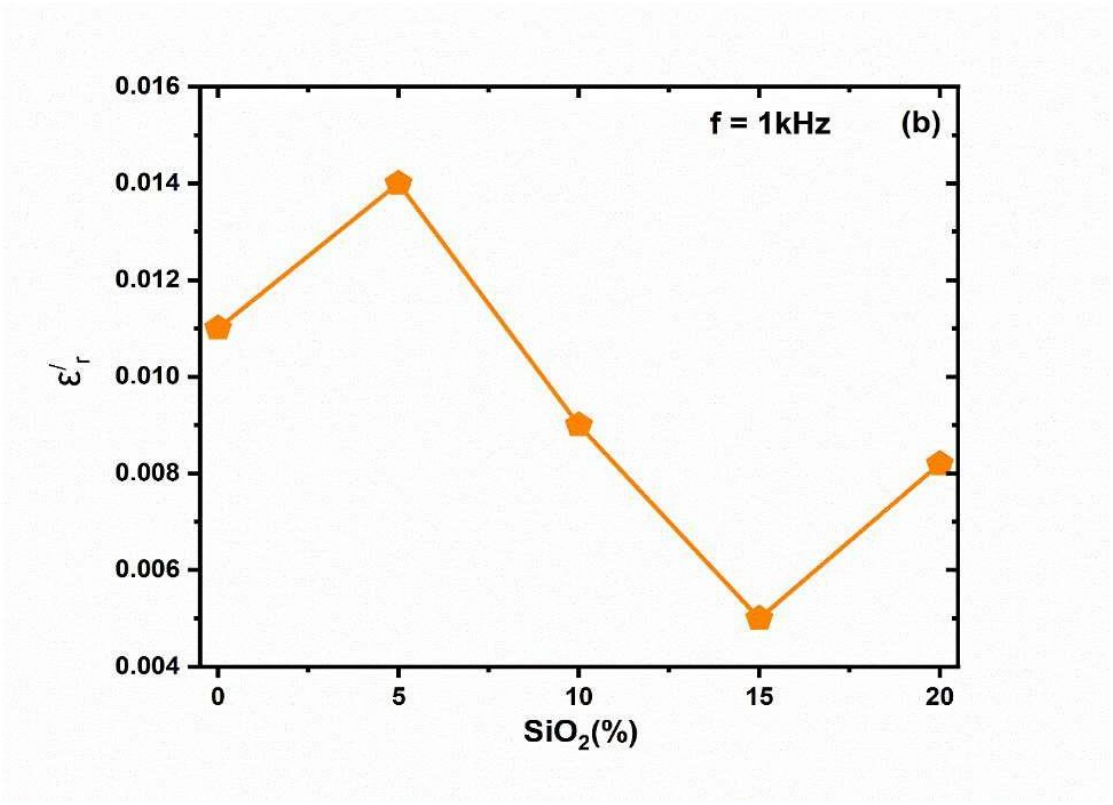

Figure 4.8: Real part of dielectric constant ($\varepsilon'r$) of $ZnFe_2O_4$ nanoparticles versus SiO_2 matrix for all samples for y = 0 wt. % ~ 20 wt. % at frequency of 1 kHz.

The real part of dielectric constant for $ZnFe_2O_4$ nanoparticles versus silica coating for all samples (y= 0 wt. % ~ 20 wt. %) was studied and analyzed in frequency range of 1kHz to 10 MHz at room temperature as shown in Fig.4.7 while Fig.4.8 indicated values of the real part of dielectric constant for versus SiO_2 coating at frequency of 1 kHz. All samples showed the values of real part of dielectric constant was high at low frequencies and had a decreasing pattern with raise in frequency and showed saturated values at higher frequencies. This behavior can be explained by Koop's theory and the Maxwell-Wegner model, which were covered in earlier sections on dielectric constants. A plot between SiO_2 concentration and values of real part of dielectric constant for all samples demonstrate in Fig. 4.8 which indicated the anomalous behavior in samples as well as segregation and stresses produced by silica matrix. Which may be due to non-uniform distribution of these nanoparticles in zinc ferrite.

4.3.4 Imaginary Part Of Dielectric Constant ($\varepsilon''r$)

The imaginary part of dielectric constant represents the energy losses within the materials. The imaginary part of dielectric constant for ZnFe2O4 nanoparticles versus

silica coating for all samples (y= 0 wt. % ~ 20 wt. %) was studied and analyzed in frequency range of 1kHz to 10 MHz at room temperature as shown in Fig.4.9 while Fig.4.10 indicated values of the imaginary part of dielectric constant for versus SiO2 coating at frequency of 1 kHz. All samples showed the values of imaginary part of dielectric constant was high at low frequencies and had a decreasing pattern accompanied by increase in frequency and showed saturated values at higher frequencies [87]. As covered in earlier sections on dielectric constants, this behavior can be explained by Koop's theory and the Maxwell-Wegner model.

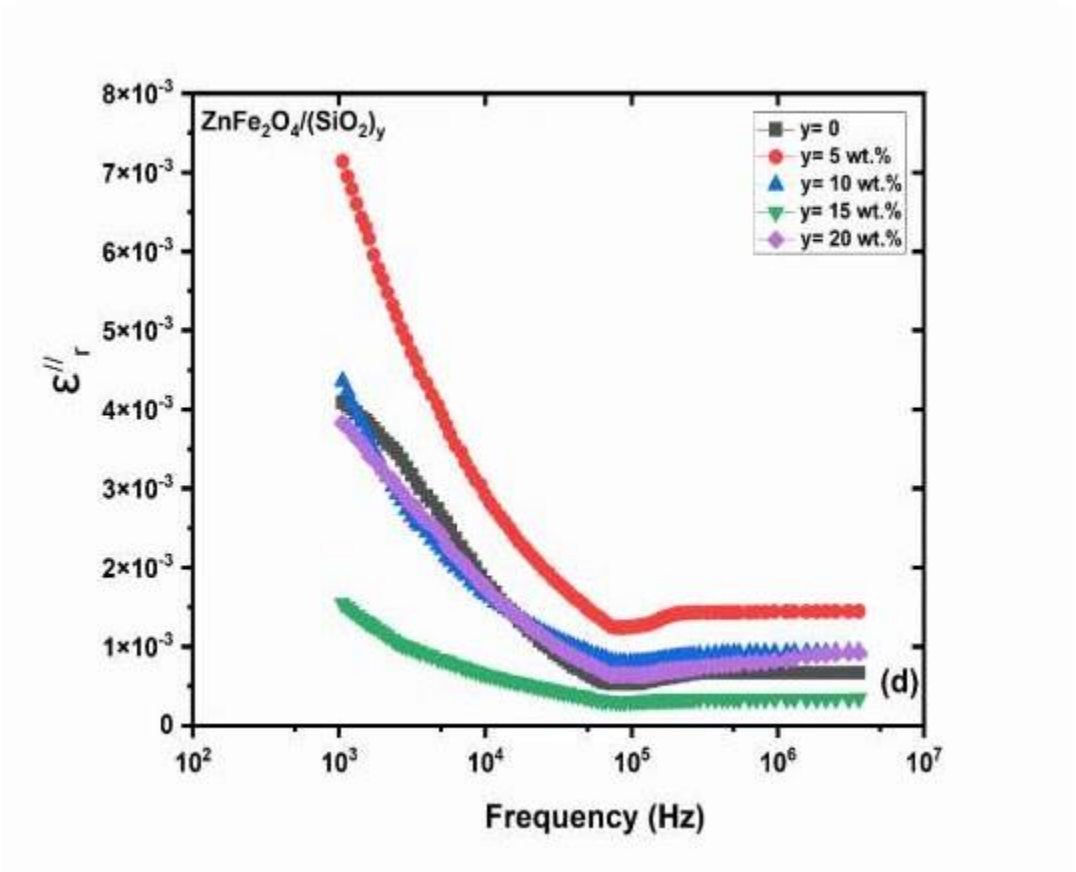

Figure 4.9: Imaginary part of dielectric constant ($\varepsilon^{//}r$) of $ZnFe_2O_4$ nanoparticles embedded with SiO_2 matrix for all samples for y = 0 wt. % ~ 20 wt. % respectively.

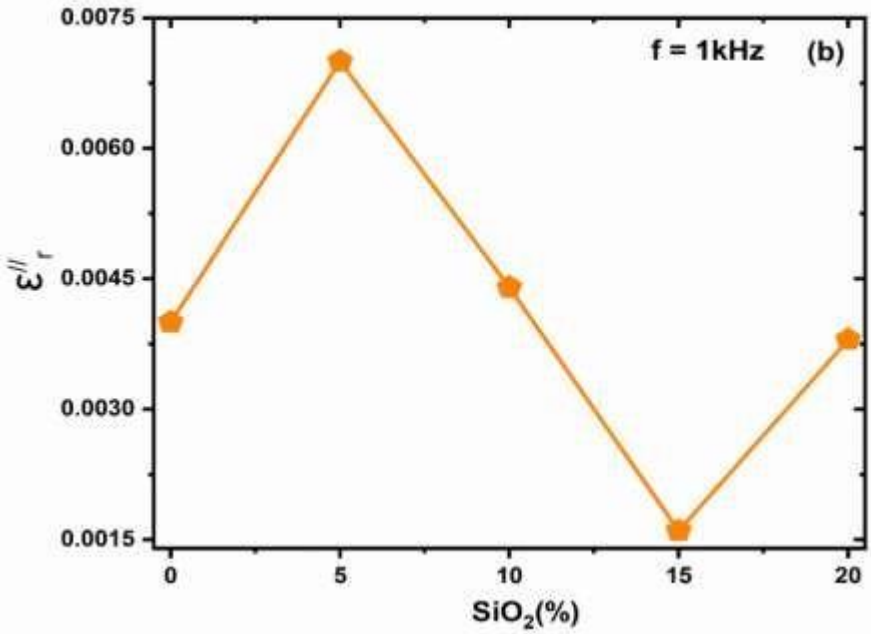

Figure 4.10: Imaginary part of dielectric constant (ε''_r) of $ZnFe_2O_4$ nanoparticles versus SiO_2 matrix for all samples for y = 0 wt. % ~ 20 wt. % at frequency of 1 kHz.

The imaginary part depends upon two factors that are the real part of dielectric constant and dissipation factors so that samples have greater values of imaginary part as compared to real part of dielectric constant. At higher frequencies, dipoles are independent of the electric field, and polarization is shown to decrease with frequency [88]. The graph showed the typical ferrite behavior for each sample as determined by the real part of the dielectric constant i.e. large dielectric constant at low frequencies and vice versa, which was exactly in accordance with Koop's theory and Maxwell Wagner model. The values of imaginary part of dielectric constant at frequency of 1 kHz versus concentration of silica matrix which indicated the anomalous behavior of these nanoparticles. This behavior may be due to random distribution of these nanoparticles between grain-boundaries.

4.3.5 Ac Conductivity

The formula presented below can be used to calculate AC conductivity.

$$\sigma_{ac} = \varepsilon' \varepsilon_0 \omega \tan\delta \qquad (4.4)$$

σ_{ac} = conductivity, ε' = real part of dielectric constant, ε_0 = permittivity of free space, $\tan\delta$ = dispersion constant, $\omega = 2\pi f$ is angular frequency.

The ac conductivity for $ZnFe_2O_4$ nanoparticles versus silica coating for all samples (y= 0 wt. % ~ 20 wt. %) was studied and analyzed in frequency range of 1kHz to 10 MHz at room temperature as shown in Fig.4.11 while Fig.4.12 indicated values of ac conductivity for zinc ferrite nanoparticles versus SiO_2 coating at frequency of 1 kHz. All samples showed the values of ac conductivity were low at low frequencies and had an increasing pattern with increase in frequency and showed increasing values at higher frequencies.

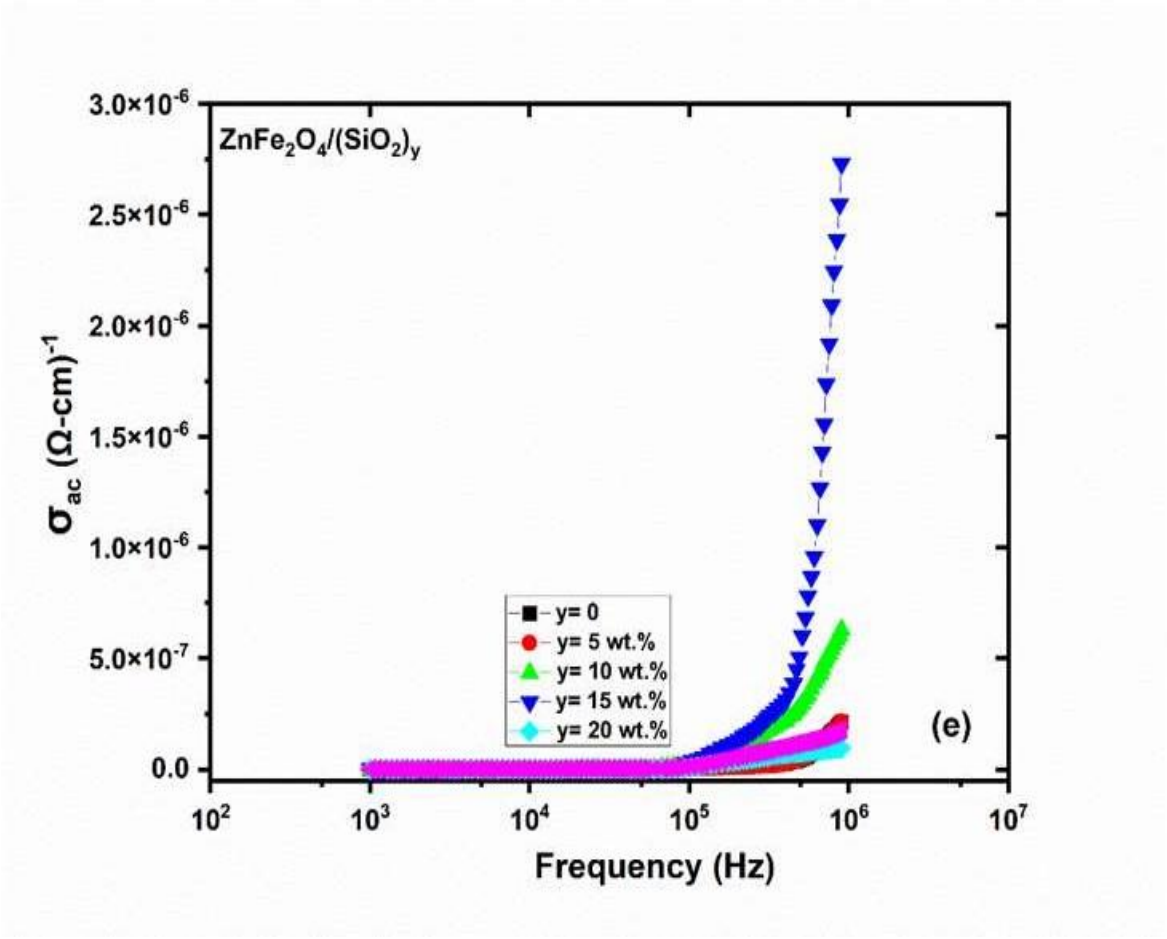

Figure 4.11: Ac conductivity (σ_{ac}) of $ZnFe_2O_4$ nanoparticles embedded with SiO_2 matrix for all samples for y = 0 wt. % ~ 20 wt. % respectively.

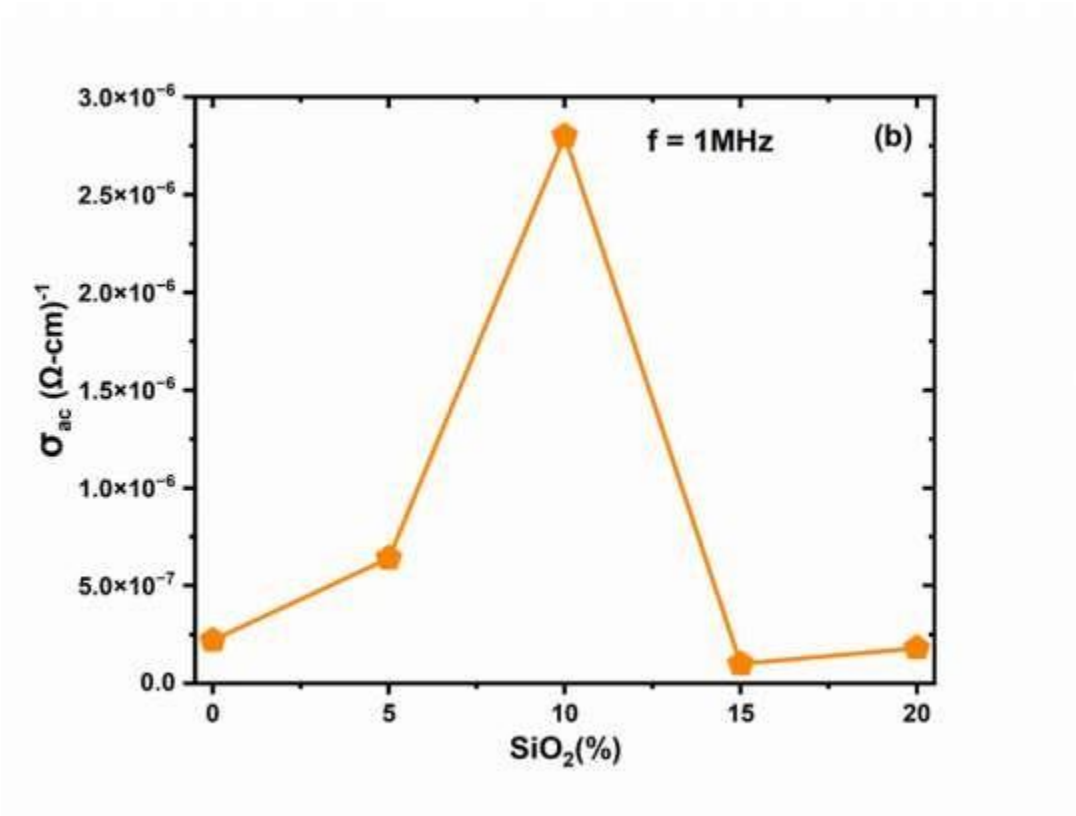

Figure 4.12: Ac conductivity (σac) of $ZnFe_2O_4$ nanoparticles versus SiO_2 matrix for all samples for y = 0 wt. % ~ 20 wt. % at frequency of 1 kHz.

The process of conductivity was observed to increase due to the increase in the large number of charge carriers which became free at higher frequencies in materials. In ferrite nanoparticles, hopping between Fe^{+2} and Fe^{+3} ions at octahedral sites, the conductance is generated. The probability of hooping depends on a few variables, such as activation energy and the distance between divalent and trivalent ions [89]. Due to the hooping mechanism between the octahedral sites, conductance occurred in ferrites. The probability of electron transformation at the different sites was observed to fall so as resulted in decrease the number of sites and hence the decrease in conductance at low frequency. Another reason for low conductivity at low frequency was due to inactivity of grain at low frequency which as a results low free charge carrier. The metallic ion separation mechanism among sites A (tetrahedral) and B (octahedral) is larger than that between two nearby sites B-B (octahedral-octahedral). There is a lower probability of hooping at sites A (tetrahedral) and B (octahedral) due to large distance between them, and a higher probability of hooping mechanism at sites B-B (octahedral-octahedral) because of small separation between them. Because A (tetrahedral) and B (octahedral) have a high potential barrier, their activation energy

is lower so that conduction happened due to electronic interchange between these sites. An increase in frequency at octahedral sites causes an increase in charge mobility. Thus, an increase in frequency results in an increase in conductivity. It was observed that all the samples showed larger conductivity at higher frequencies because of the hopping mechanism between Fe^{+2} and Fe^{+3}. The major factor that influenced the hopping process and conductivity in our samples was energy activation. Since there is more space between sites A (tetrahedral) and B (octahedral) than between sites B-B (octahedral-octahedral), therefore is more chance of hopping between sites B-B (octahedral-octahedral) than between sites A (tetrahedral) and B (octahedral) [90,91]. The mobility of charges in ferrites determines the electronic exchange rate. Therefore, an increase in frequency leads to an increase in the exchange rate, which in turns caused greater conductivity at higher frequency. It can be explained by a phase shift with changing SiO_2 concentration in these $ZnFe_2O_4$ nanoparticles, which showed the non-monotonic behavior with increasing SiO_2 concentration [92].

CONCLUSIONS

Zinc ferrite nanoparticles ($ZnFe_2O_4$) were synthesized with the help of sol-gel route coated with different concentration of SiO_2 matrix such as 0 wt. %, 5 wt. %, 10 wt. %, 15 wt. %, and 20 wt. %, (y= 0 ~20 wt. %) $ZnFe_2O_4/(SiO_2)y\}$. The structural properties were investigated by x-rays spectroscopy (XRD) while morphology was studied with help of scanning electron microscopy (SEM) and elemental study via EDX spectroscopy. It was observed that crystallite size was observed to decrease with increase SiO_2 contents which restricted the nucleation growth of Zinc ferrite nanoparticles. The lattice parameters also decreased due to increasing concentration of silica matrix. The XRD results showed the non-monotonic behavior of these nanoparticles due to stresses as well as due to agglomeration and segregation produced by silica matrix during synthesis process. The results of scanning electron microscope indicated the different shape of nanoparticles such as spherical, rod shape with regular as well as ir-regular symmetry. The EDX results indicated that all elements like Fe, Zn, O, C and Si and their peaks in appropriate ratios were present. Dielectric studies showed that conductivity represents reciprocal behavior and that parallel plate capacitance, the real and imaginary parts of the dielectric constant, as well as loss tangents, were observed to decrease with increasing frequency. All these parameters of dielectric study showed an anomalous behavior with increasing SiO_2 concentration that could be elaborated with Koop's theory and Maxwell-Wagner model. The values of dielectric parameters at higher frequencies were found to decrease and suppressed because the dipole moment was unable to follow the applied electric field except conductivity. The samples of zinc ferrite nanoparticles coated with silica matrix showed anomalous behavior due to stress and strain produced during synthesis process. In conclusion, the structural, optical, and dielectric properties of zinc ferrite nanoparticles are significantly influenced by the concentration of silica matrix which are beneficial for high energy storage materials.

REFERENCES

1. Ahmad A, Senapati S, Khan M. I, Kumar R, Ramani R, Srinivas v, et al. Intracellular synthesis of gold nanoparticles by a novel alkalotolerant actinomycete. J Rhodococcus species. (2003); Nanotechnology 14(824): 0957-4484.
2. Ahmad T, Wani I. A, Ahmed J, and Al-Hartomy O. A. Effect of gold ion concentration on size and properties of gold nanoparticles in TritonX-100 based inverse microemulsions. J Appl. Nanosci. (2014); 4: 491–498.
3. Ajitha B, Reddy Y. A. K, and Reddy P. S. Green synthesis and characterization of silver nanoparticles using Lantana camara leaf extract. J Mater. Sci. Eng. (2015); 49: 373–381.
4. Al-Dhabi N. A, Mohammed Ghilan, A.K, and Arasu M. V. Characterization of silver nanomaterials derived from marine Streptomyces sp. al-dhabi-87 and its in vitro application against multidrug resistant and extended-spectrum beta-lactamase clinical pathogens. J Nanomaterials. (2018); 8(279).
5. Amendola V, and Meneghetti M. Laser ablation synthesis in solution and size manipulation of noble metal nanoparticles Phys.J Chem. Chem. Phys. (2009); 11:3805–3821.
6. Anjum S, Hashim M, Malik S. A, Khan M, Lorenzo J. M, Abbasi B. H, et al. Recent advances in zinc oxide nanoparticles (ZnO NPS) for cancer diagnosis, target drug delivery, and treatment. J Cancers (2021); 13:4570-4578.
7. Astefanei A., Núñez O, and Galceran M. T. Characterization and determination of fullerenes: a critical review. J Anal. Chim. (2015); 7(56): 882-890.
8. Bahadur P. S, Jaiswal S, Srivastava R, and Kumar A. (2021). Advanced application of nanotechnology in engineering. J Mater.Adv. (2021); 43: 92–95.
9. Baig N, Kammakakam I, and Falath W. Nanomaterials: A review of synthesis methods, properties, recent progress, and challenges. j Mater. Adv. (2021); 2: 1821– 1871.
10. Banerjee A, Krishna R, and Das B. Size controlled deposition of Cu and Si

nanoclusters by an ultra-high vacuum sputtering gas aggregation technique. j Appl. Phys. A (2008);90: 299–303.

11. Bayda S, Adeel M, Tuccinardi T, Cordani M, and Rizzoli F. The history of nanoscience and nanotechnology: from chemical–physical applications to nanomedicine. j Molecules (2019); 25:112.
12. Behrisch R. Sputtering by Particle Bombardment Springer Verlag. J Berlin-Heidelberg: Springer. (1981); 76(6): 609-765.
13. Berkman's A. J, Jagannatham M, Priyanka S, and Haridoss P. Synthesis of branched, nano channeled, ultrafine and nano carbon tubes from PET wastes using the arc discharge method. J Waste Manag. (2001); 34: 2139–2145.
14. Beyene H. D, Werkneh A. A, Bezabh H. K, and Ambaye, T. G. Synthesis paradigm and applications of silver nanoparticles (AgNPs), a review. J Sustain. Mater. Technol. (2017); 13: 18–23.
15. Bhattacharjee S.DLS and zeta potential–what they are and what they are not? J. Control. (2016); 235: 337–351.
16. Bhavani K. S, Anusha T, and Brahman P. K. Platinum nanoparticles decorated on graphitic carbon nitride-ZIF-67 composite support: An electrocatalyst for the oxidation of butanol in fuel cell applications. Int. J Hydr Energy (2021); 46: 9199– 9214.
17. Biju V, Itoh T, Anas A, Sujith A and Ishikawa M. Semiconductor quantum dots and metal nanoparticles: syntheses, optical properties, and biological applications. J Anal. Bioanal. Chem. (2008);391: 2469–2495.
18. Brady B, Wang P. H, Steenhoff V, and Brolo A. G. Nano structuring solar cells using metallic nanoparticles, in Metal Nanostructures for Photonics, eds L. R. P. Kassab, and C. B. De Araujo (Amsterdam: Elsevier). J Nature Res. (2019); 65:197– 221.
19. 19: Cadene A, Durand-Vidal S, Turq P, and Brendle J. Study of individual Na-montmorillonite particles size, morphology, and apparent charge. J. Colloid Interf. Sci. (2008); 285: 719–730.
20. 20: Chen J, and Zhu X. Magnetic solid phase extraction using ionic liquid-coated core–shell magnetic nanoparticles followed by high-performance liquid

chromatography for determination of Rhodamine B in food samples. j Food Chem. (2016);200: 10–15.

21. Chen J, Guo Y, Zhang X, Liu J, Gong P, Su Z, et al. Emerging nanoparticles in food: sources, application, and safety. J. Agricult. Food Chem. (2023);71: 3564–3582.
22. Chen J, Wei S, and Xie H. A brief introduction of carbon nanotubes: history, synthesis, and properties, in Proceedings of the Journal of Physics: Conference Series, (United Kingdom: IOP Publishing), 012184.
23. Chen J.-C, and Tang C.-T. Preparation and application of granular ZnO/Al_2O_3 catalyst for the removal of hazardous trichloroethylene. J. Hazardous Mater. (2007); 142: 88–98.
24. Chronakis I. S. Micro-/nanofibers by electrospinning technology: processing, properties and applications. J Micromanufact. Eng. Technol. (2010); 65: 264–286.
25. Compostella F, Pitirollo O, Silvestri A, and Polito L. Glyco-gold nanoparticles: synthesis and applications. Beilstein. J Org. Chem. (2017);13: 1008–1021.
26. Dahoumane S. A, Mechouet M, Wijesekera K, Filipe C. D, Sicard C, Bazylinski
27. D. A, et al. Algae-mediated biosynthesis of inorganic nanomaterials as a promising route in nanobiotechnology–a review. J Green Chem. (2017);19: 552–587.
28. Dangi K, and Verma A. K. Efficient & eco-friendly smart nano-pesticides: Emerging prospects for agriculture. J Mater. Today Proc. (2021);45: 3819–3824.
29. Das S, and Srivastava V. C. Synthesis and characterization of ZnO–MgO nanocomposite by co-precipitation method. J Smart Sci. (2016); 4: 190–195.
30. De La Calle I, Menta M, Klein M, and Séby F. Study of the presence of micro- and nanoparticles in drinks and foods by multiple analytical techniques. J Food Chem. (2018); 266: 133–145.

31. Delvalle A, Feltin N, Ducourtieux S, Trabelsi M, and Hochepied J. Direct comparison of AFM and SEM measurements on the same set of nanoparticles. J Measur. Sci. Technol. (2015); 26: 085601.

32. Dhand V, Soumya L, Bharadwaj S, Chakra S, Bhatt D, and Sreedhar B. Green synthesis of silver nanoparticles using Coffea arabica seed extract and its antibacterial activity. J Mater. Sci. Eng. (2016); 58: 36–43.

33. Dikusar A, Globa P, Belevskii S, and Sidel'nikova S. On limiting rate of dimensional electrodeposition at meso-and nanomaterial manufacturing by template synthesis. J Surf. Eng. Appl. Electrochem. (2009); 45: 171–179.

34. Dragovic R. A, Gardiner C, Brooks A. S, Tannetta D. S, Ferguson D. J, Hole P, et al. Sizing and phenotyping of cellular vesicles using nanoparticle tracking analysis. J Nanomedicine. (2011); 7: 780–788.

35. Dreaden E. C, Alkilany A. M, Huang X, Murphy, C J and El-Sayed M. A. The golden age: gold nanoparticles for biomedicine. J Chem. Soc. Rev. (2012); 41: 2740– 2779.

36. Du P, Song L, Xiong J, Li N, Xi Z, Wang L, et al. Coaxial electrospun TiO2/ZnO core–sheath nanofibers film: Novel structure for photoanode of dye-sensitized solar cells. J Electrochim. (2012); 78: 392–397.

37. Edison T. N. J. I, Lee Y. R, and Sethuraman M. G. Green synthesis of silver nanoparticles using Terminalia cuneata and its catalytic action in reduction of direct yellow-12 dye. J Pectrochimica Acta Part A. (2016); 161: 122–129.

38. Elliott J. A, Shibuta Y, Amara H, Bichara C, and Neyts E. C. Atomistic modelling of CVD synthesis of carbon nanotubes and graphene. J Nanoscale (2013); 5: 6662– 6676.

39. Erasmus M, Cason E. D, Van Marwijk J, Botes E, Gericke M, and Van Heerden

40. E. Gold nanoparticle synthesis using the thermophilic bacterium Thermus scotoductus SA-01 and the purification and characterization of its unusual gold reducing protein. J Gold Bull. (2014);47: 245–253.

41. Eroglu E, Chen X, Bradshaw M, Agarwal V, Zou J, Stewart S. G, et al. Biogenic production of palladium nanocrystals using microalgae and their

immobilization on chitosan nanofibers for catalytic applications. J RSC Adv. (2013); 3: 1009–1012.

42. Essajai R, Benhouria Y, Rachadi A, Qjani M, Mzerd A, and Hassanain N. Shape- dependent structural and magnetic properties of Fe nanoparticles studied through simulation methods. J RSC Adv. (2019); 9: 22057–22063.
43. Falke S, and Betzel C. Dynamic light scattering (DLS), in Radiation in Bioanalysis, eds A. S. Pereira, P. Tavares, P. Limão-Vieira. J Springer (2019); 65: 173–193.
44. Farrell D, Majetich S. A, and Wilcoxon J. P. Preparation and characterization of monodisperse Fe nanoparticles. J. Phys. Chem. (2003); 107: 11022–11030.
45. Feng L, Xuan Z, Ma J, Chen J, Cui D, Su C, et al. Preparation of gold nanorods with different aspect ratio and the optical response to solution refractive index. J. Exp. Nanosci. (2015); 10: 258–267.
46. Ghorbani H. R, Mehr F. P, Pazoki H, and Rahmani B. M. Synthesis of ZnO nanoparticles by precipitation method. Orient. J. Chem. (2015); 31: 1219–1221.
47. Ghosh S, Ahmad R, Zeya Ullah M, and Khare S. K. Microbial nano-factories: synthesis and biomedical applications. J Front. Chem. (2021); 9: 194-200.
48. Giljohann D. A, Seferos D. S, Daniel W. L, Massich M. D, Patel P. C, and Mirkin
49. C. A. Gold nanoparticles for biology and medicine. J Spherical Nucleic Acids. (2020); 49: 3280–3294.
50. Giurlani W, Innocenti M, and Lavacchi A. X-ray microanalysis of precious metal thin films: thickness and composition determination. J Coatings (2018); 8: 84-90.
51. Gloria E. C, Ederley V, Gladis, M, César H, Jaime O, Oscar A, et al. Synthesis of silver nanoparticles (AgNPs) with antibacterial activity. in Proceedings of the Journal of Physics: Conference Series, (United Kingdom: IOP Publishing). (2017); 5: 880- 902.
52. 49: Gorrasi G, and Sorrentino A. Mechanical milling as a technology to

produce structural and functional bio-nanocomposites. J *Green Chem.* (2015);17: 2610–2625.

53. Govindarajan M, Rajeswary M, Veerakumar K, Muthukumaran U, Hoti S, and Benelli G. Green synthesis and characterization of silver nanoparticles fabricated using Anisomeles indica: mosquitocidal potential against malaria, dengue and Japanese encephalitis vectors. J Exp. Parasitol. (2016); 161: 40–47.

54. Graf C, Vossen D. L, Imhof A, and Van Blaaderen A. A general method to coat colloidal particles with silica. J Langmuir. (2003); 19: 6693–6700.

55. Greczynski G, and Hultman L. X-ray photoelectron spectroscopy: towards reliable binding energy referencing. J Progr. Mater. Sci. (2020); 107: 555-560.

56. Guo D, Xie G, and Luo J. Mechanical properties of nanoparticles: basics and applications. J. Phys. D. (2013); 47: 770-800.

57. Guo W, Pleixats R, and Shafir A. Water-soluble gold nanoparticles: from catalytic selective Nitroarene reduction in water to refractive index sensing. Chem. An Asian J. (2015); 10: 2437–2443.

58. Gwynne K. Enhancement of the Photostability of Blue Phosphorescence Using Plasmonic Surfaces. J New Brunswick, NJ: Rutgers University-School of Graduate Studies. (2020).

59. Haasch R. T. X-ray photoelectron spectroscopy (XPS) and auger electron spectroscopy (AES), in Practical Materials Characterization, Ed. M. Sardela. J (Berlin: Springer). (2014); 12: 93–132.

60. Hasan S. A review on nanoparticles: their synthesis and types. Res. J. Recent Sci. (2015); 2277: 2502-2506.

61. Holder C. F, and Schaak R. E. Tutorial on Powder X-ray Diffraction for Characterizing Nanoscale Materials. J Washington. (2019).

62. Hollamby M. J, Eastoe J, Chemelli A, Glatter O, Rogers S, Heenan R. K, et al. Separation and purification of nanoparticles in a single step. J Langmuir. (2019); 26: 6989–6994.

63. Hoo C. M, Starostin N, West P, and Mecartney M. L. A comparison of atomic

force microscopy (AFM) and dynamic light scattering (DLS) methods to characterize nanoparticle size distributions. J. Nanopart. Res. (2008); 10: 89–96.

64. Hortin J, Anderson A, Britt D, Jacobson A, and Mclean J. Copper oxide nanoparticle dissolution at alkaline pH is controlled by dissolved organic matter: influence of soil-derived organic matter, wheat, bacteria, and nanoparticle coating. Environ. Sci. (2020); 7: 2618–2631.

65. Hoseinzadeh E, Makhdoumi P, Taha P, Hossini H, Stelling J, and Amjad Kamal

66. M.A review on nano-antimicrobials: metal nanoparticles, methods and mechanisms. Curr. Drug Metab. (2017); 18: 120–128.

67. Islam F, Shohag S, Uddin M. J, Islam M. R, Nafady M. H, Akter A, et al. Exploring the journey of zinc oxide nanoparticles (ZnO-NPs) toward biomedical applications. Materials (2020); 15:2160.

68. Jadoun S, Arif R, Jangid N. K, and Meena R. K. Green synthesis of nanoparticles using plant extracts: A review. Environ. Chem. Lett. (2021); 19: 355–374.

69. Jamkhande P. G, Ghule N. W, Bamer A. H, and Kalaskar M. G. Metal nanoparticles synthesis: An overview on methods of preparation, advantages and disadvantages, and applications. J. Drug Deliv. Sci. Technol. (2021); 53: 101174.

70. Jana N. R, Earhart C, and Ying J. Y. Synthesis of water-soluble and functionalized nanoparticles by silica coating. Chem. Mater. (2007); 19: 5074–5082.

71. Jaskulski D., Jaskulska I, Majewska J, Radziemska M, Bilgin A, and Bortnick M. Silver Nanoparticles (AgNPs) in urea solutions in laboratory tests and field experiments with crops and vegetables. Materials (2020); 15:870.

72. Jayaraman V, Ghosh S, Sengupta A, Srivastava S, Sonawat H, and Narayan P. K. Identification of biochemical differences between different forms of male infertility by nuclear magnetic resonance (NMR) spectroscopy. J. Assist. Reproduct. Genet. (2014);31: 1195–1204.

73. Jena J, Pradhan N, Nayak R. R, Dash B. P, Sukla L. B, Panda P. K, et al. Microalga Scenedesmus sp.: a potential low-cost green machine for silver nanoparticle synthesis. J. Microbiol. Biotechnol. Adv. (2014); 24: 522–533.

74. Jiang H.-L, and Xu Q. Catalytic hydrolysis of ammonia borane for chemical hydrogen storage. Catal. Today (2011);170: 56–63.

75. Joh D.-W, Jung T.-K, Lee H.-S, and Kim D.-H. Synthesis of nanoparticles using electrical explosion of Ni wire in Pt solution. J. Nanosci. Nanotechnol. (2013);13: 6092–6094.

76. Kahle M., Kleber M, and Jahn R. Review of XRD-based quantitative analyses of clay minerals in soils: the suitability of mineral intensity factors. Geoderma (2002); 109: 191–205.

77. Kalaiyarasu T, Karthi N, Sharmila G. V, and Manju V. In vitro, the assessment of antioxidants and antibacterial activity of green synthesized silver nanoparticles from Digitaria radicosa leaves. Asian J. Pharm. Clin. Res. (2016); 9: 297–302.

78. Ai Z, Deng K, Wan Q, Zhang L, Lee S. Facile microwave-assisted synthesis and magnetic and gas sensing properties of Fe3O4 nanoroses. J Phys Chem C (2010); 114: 6237.

79. A, Zafar H, Zia M, Haq I, Phull AR, Ali JS, Hussain A. Synthesis, characterization, applications, and challenges of iron oxide nanoparticles. Nanotechnol Sci App (2016); 9:49–67.

80. Ansari MO, Ahmad F, Parveen N, Ahmad S, Jameel S, Shadab CGHA. Iron oxide nanoparticles-synthesis, surface modification, applications and toxicity: a review. Mater Focus (2017) ;6 :1 -11.

81. Arias LS, Pessan JP, Miranda-Vieira A, Lima T, Delbem A, Monteiro DR. Iron oxide nanoparticles for biomedical applications: a perspective on synthesis, drugs, antimicrobial activity, and toxicity. Antibiotics (2017); 7: 46.

82. Avazzadeh R, Farahani EV, Soleimani M, Amanpour S, Sadeghi M. Synthesis and application of magnetite dextran-spermine nanoparticles in breast cancer hyperthermia. Prog Biomater (2017); 6:75–84.

83. Bae H, Ahmad T, Rhee I, Chang Y, Jin SU, Hong S. Carbon-coated iron oxide

nanoparticles as contrast agents in magnetic resonance imaging. Nanoscale Res Lett (2012); 5(7):44.

84. Bahadur A, Saeed A, Shoaib M, Iqbal S, Bashir MI, Waqas M, Hussain MN, Abbas

85. N. Eco-friendly synthesis of magnetite (Fe_3O_4) nanoparticles with tunable size: dielectric, magnetic, thermal and optical studies. Mater Chem Phys (2017); 198:229– 235.

86. Balivada S, Rachakatla RS, Wang H, Samarakoon TN, Dani RK, Pyle M, Kroh F, Walker B, Leaym X, Koper OB, Tamura M, Chikan V, Bossmann SH, Troyer DL.

87. A/C magnetic hyperthermia of melanoma mediated by iron oxide core/shell magnetic nanoparticles: a mouse study. BMC Cancer (2019); 10:119.

88. Barahuie F, Dorniani D, Saifullah B, Gothai S, Hussein MZ, Pandurangan AK, Arulselvan P, Norhaizan ME. Sustained release of anticancer agent phytic acid from its chitosan-coated magnetic nanoparticles for drug-delivery system. Int J Nanomed (2016); 12:2361–2372.

89. Barrow M, Taylor A, Murray P, Rosseinskya MJ, Adams DJ. Design considerations for the synthesis of polymer coated iron oxide nanoparticles for stem cell labelling and tracking using MRI. Chem Soc Rev (2015); 44:6733–6748.

90. Bee A, Massart R, Neveu S. Synthesis of very fine maghemite particles. J Magn Magn Mater (1995); 149:6–9.

91. Billotey C, Wilhelm C, Devaud M, Bacri JC, Bittoun J, Gazeau F. Cell internalization of anionic maghemite nanoparticles: Quantitative effect on magnetic resonance imaging. Magn Reson Med Sci (2003) ;49: 646–654.

92. Biswas A, Bayer IS, Biris AS, Wang T, Dervishi E, Faupel F. Advances in top– down and bottom–up surface nanofabrication: techniques, applications & prospects. Adv Colloid Interface Sci (2012); 170: 2–27.

93. Bitar A, Kaewsaneha C, Eissa MM, Jamshaid M, Tangboriboonrat T, Polpanich P, Elaissari D. Ferrofluids: from preparation to biomedical applications. J Colloid Sci Biotechnol (2014); 3:3 18.

94. Carrey J, Mehdaoui B, Respaud M. Simple models for dynamic hysteresis loop calculations of magnetic single-domain nanoparticles: application to magnetic hyperthermia optimization. J Appl Phys (2011); 109: 083921.

95. Chentamara D, Subramaniam S, Ramakrishnan SG, Krishnaswamy S, Essa MM, Lin FH, Qoeonfleh MW. Therapeutic efficacy of nanoparticles and routes of administration. Biomater Res (2019); 23:20.

96. Chouly C, Pouliquen D, Lucet I, Jeune JJ, Jallet P. Development of superparamagnetic nanoparticles for MRI: effect of particle size, charge and surface nature on biodistribution. J Microencapsul (1996); 13:245–255.

97. Costo R, Morales MP, Veintemillas-Verdaguer S. Improving magnetic properties of ultrasmall magnetic nanoparticles by biocompatible coatings. J Appl Phys (2015); 117:6.

98. Cui X, Dong L, Zhong S, Shi C, Sun Y, Chen P. Sonochemical fabrication of folic acid functionalized multistimuli-responsive magnetic graphene oxide-based nanocapsules for targeted drug delivery. Chem Eng J (2017); 326:839–848.